SYNTHESIS AND CHARACTERIZATION OF ULTRATHIN BLACK PHOSPHORUS

KAM TSZ YAU

MPhil

The Hong Kong Polytechnic University

2022

The Hong Kong Polytechnic University

Department of Applied Physics

Synthesis and Characterization of Ultrathin Black Phosphorus

KAM TSZ YAU

A thesis submitted in partial fulfillment of the

requirements for the degree of Master of Philosophy

August 2021

Certificate of Originality

I hereby declare that this thesis is my own work and that, to the best of my knowledge and belief, it reproduces no material previously published or written nor material which has been accepted for the award of any other degree or diploma, except where due acknowledgement has been made in the text.

_____(Signature)

_____Kam Tsz Yau_____(Name of candidate)

Abstract

Two-dimensional materials attract much attention from material scientists due to their unique physical and optical properties. Graphene and transition metal dichalcogenides are examples of widely studied 2D materials. Black Phosphorus (BP), namely phosphorene, is an emerging candidate in this field. It has a thickness-dependent energy bandgap ranging from 0.3 eV to 2.0 eV in bulk to monolayer and high carrier mobility, making it an excellent choice for optoelectronics applications. Furthermore, the unique A17 orthorhombic crystal structure of BP with weak interlayer van der Waals force also provides the anisotropic behaviour in BP along with the zigzag (ZZ) and armchair (AC) directions. This anisotropy makes it a great thermoelectric and piezoelectric candidate.

In this study, BP crystals were synthesized by the chemical vapour transportation method. Red phosphorus, tin, and iodine were used as precursors and heated in a vacuum-sealed quartz tube to produce BP. It was then mechanically exfoliated for characterization. Small Raman shift in bulk and exfoliated BP was observed, and anisotropy polarised Raman was measured. Single crystal quality and high purity of BP were confirmed by selected area electron diffraction and energy dispersive x-ray in the transmission electron microscope observation.

Molecular beam epitaxy BP synthesis was attempted by using GaP source and mica substrate with a fast cooling after growth. Raman spectroscopy, atomic force microscopy, and x-ray diffraction characterized the large area thin film uniformity and crystalline structure.

The strain-induced electrical conductance of BP in ZZ and AC orientations was also

investigated. Conductance (G) of 4.43μS and 1.01 μS were observed in the AC and ZZ directions, with a ratio G_{ac}/G_{zz} of 4.4 without strain. Conductance along ZZ and AC were also measured with applied 0 - 1.4% uniaxial strain in either ZZ or AC direction. In most cases, the conductance drops exponentially to about 20% of the original value at 1.4% strain except the conductance of ZZ orientation when applying strain in the same direction, which is half of its original. Results suggested that the unique conductance behaviour in ZZ direction with uniaxial ZZ strain could be attributed to the spatial preference transition of electrical conductance in BP.

Acknowledgements

I would like to express my sincere gratitude to my supervisor, Prof. S. P. Lau, for his guidance and supervision. He provided many valuable suggestions and showed patience when I encountered obstacles during my research.

Huge thanks are also given to my senior research team members, Dr Y. Y. Li, for the cooperation and assistance on the strain effect measurement on the flexible BP device, and Dr. Y. C. Liu for the suggestions and characterization of 2D MBE synthesis. Also, thanks to Dr. C. H. Mak, Dr. L. Rogée, and Mr. W. K. Lai for the advice and assistant in my research life.

Appreciation is also given to Dr. Terence Wong, Ms. Joyce Lau, and Dr. H. F. Wong, for the technical and equipment support in the Department of Applied Physics and the University Research Facility in Materials Characterization and Device Fabrication.

Last but not least, I would like to thank my family for understanding and supporting me through these years. They listened to me when I was stressed and cheered me up when I doubted. They provided me with the energy to keep driving forward.

Table of Contents

List of Figures

List of Tables

Chapter 1 Introduction

1.1 Background

In the 21st century, two dimensional (2D) materials have attracted much attention due to their relatively faster, efficient and lower power consumption device performance than that of the bulk material. Graphene, the first 2D material, had been proposed in the 18th century and was only realized until 2004 [1]. It was believed that 2D compounds should not exist since the separation of the layers would create thermal instability in the crystal. However, two researchers at the University of Manchester, Professor Andre Geim and Professor Kostya Novoselov, successfully exfoliated graphene from graphite, proving the existence of 2D material is probable. It was later found out that exfoliated 2D material has weak van der Waals or electrostatic out-of-plane interactions together with a strong covalent or ionic in-plane bond [2]. Thus, isolating 2D material from the bulk was proven to be achievable.

Many materials were exfoliated to their 2D form to understand better their unique properties, such as graphene, GaSe, MoS_2, MnO_2, and black phosphorus (BP). Studies based on 2D materials have created various valuable applications. For example, MoS_2 has an energy bandgap varying with different thicknesses [3], and it was applied to photovoltaic [4], photodetector [5], and light emitters [6]. Graphene, a single atomic layer of graphite that has

zero energy gap, was utilized in advanced solar cells [7], batteries [8], and supercapacitors [9].

In 2014, the first BP, phosphorene, was successfully exfoliated and analyzed [10]. Since then, material scientists have rapidly increased attention towards this new 2D semiconducting material. BP is a rare but stable allotrope of all phosphorous materials. It was first produced in 1914 by the high temperature and high-pressure method [11]. It has an anisotropic characteristic due to its unique asymmetry A17 crystal structure [12], which has a zigzag (ZZ) and an armchair (AC) direction. It also has a direct energy bandgap between 0.3 eV to 2.0 eV for bulk to monolayer [13]. Many scholars suggested that BP is a promising candidate for complementing graphene's deficiencies since it has an energy bandgap between zero-gap graphene and large energy gap transition metal dichalcogenides (TMDs) [13]. Therefore, BP is particularly useful for infrared photonics and optoelectronics applications.

BP can be synthesized based on a high-pressure route by subjecting white phosphorus (WhiteP) to 1.2 GPa and 473 K [11]. A similar approach using red phosphorus (RP) to replace WhiteP was later reported [14]. There are many methods to produce BP crystals. For example, mechanical milling [15], bismuth-flux [16], and mineralization methods [17] are some common synthesis routes for BP growth. Recently, chemical vapour transport (CVT)

has become a more widely adopted approach to synthesize BP crystal and research suggested that it is a reliable way to produce single-crystal quality BP[18].

In the more trending development of 2D and nanomaterials, 2D BP caught more attention than its bulky form. It was manifested mainly by exfoliations such as mechanical exfoliation [1], liquid-phase exfoliation[19]–[23], and electrochemical exfoliation [29,30]. A few scholars then suggested that 2D BP can be fabricated by bottom-up synthesis instead of the traditional top-down approach. Chemical vapour deposition (CVD) produced micrometers size BP flakes with limited uniformity was reported by Smith *et al.* [26].

Yang *et al*. proposed that pulsed laser deposition (PLD) growth of centimeter scale 2D BP was feasible [27], and later, Wu [28] improved the quality of PLD growth 2D BP by adopting a dry N_2 gas rapid-cooling approach. Similarly, MBE growth of blue phosphorus (BlueP), an allotrope of BP, was performed successfully [29]–[32].

In addition, the unique and direction-dependent lattice structure of BP makes it a surprising piezoelectric material despite its monoelemental nature[33]. The piezoelectric properties in ZZ and AC directions were reported previously[34], [35]. Furthermore, the strain-induced Raman shift [36] was also studied. A theoretical study also stated that the preferred electrical conductance of BP in the AC direction could be switched to the ZZ direction based on the manipulation of mechanical strain along the ZZ direction of BP [37]. Although the current

responses due to the piezoelectric and piezo-resistive characteristics were studied, the analysis of the conductance of BP under uniaxial strain is still limited.

1.2 Motivation

Both CVD and PLD bottom-up synthesis of 2D BP were studied by various research groups [26]–[28]. In addition, the state-of-the-art MBE was used to produce 2D BlueP [29]–[32]. Since BP is in the same elemental family as BlueP, the possibility of using MBE to grow 2D BP was carried out in this study. It aims to find an alternative way to produce large and uniform BP thin films to provide a broader range of choices in the epitaxial growth of BP. A scalable, automatic, and repeatable synthesis of large-area 2D BP could be essential for the manufacture of BP devices for industrial and commercial usage in the future to utilize the excellent electrical and optical properties of BP.

Only a few scientists studied the atypical electrical anisotropy of BP, which is a rarity in 2D material. In previous research, Li *et al.* [36] found that the Raman shift of BP due to uniaxial bending strain is significant. In addition, the theoretical study of Fei and Yang [37] also suggested that the electrical conductance few-layer BP can be manipulated by strain engineering. Due to the reason above, the strain-induced effect on the electrical conductance of BP will be explored in this research. The spatial preference of the electrical conductance in both AC and ZZ directions related to strain will be discussed.

This can be beneficial to developing mechanical-electronic device applications, especially in the stretchable 2D semiconductor.

1.3 Thesis overview

In this research, the BP single crystal was produced by the CVT method. The characterization of its crystal quality was then carried out. Afterwards, it was exfoliated to fabricate a flexible BP device to analyze its conductance under different strains. The as-produced BP was then used in the MBE to grow BP thin films. Finally, the characterization of the grown MBE thin film was also made. The following is an outline of each chapter in this thesis:

Chapter 1 – An introduction to 2D materials. The physical, optical, and electrical properties of BP was briefly discussed. It is followed by an overview of the synthesis methods of bulk BP crystal and 2D BP. The motivation and significance of this study are then explained. It ends with an outline of each chapter of this thesis writing.

Chapter 2 – A literature review. The basic atomic structure of phosphorus material is provided. The descriptions of BP and the allotropes of BP are given. Next, the optical properties and electrical properties of BP are reviewed. The corresponding change in properties due to strain is also studied. After that, the synthesis methods of BP are compared. At last, the CVD and PLD growth of BP together with the MBE growth of

BlueP are summarized.

Chapter 3 – The method used in this research is explained. The CVT synthesis details and the characterization using Raman and transmission electron microscopy (TEM) are presented. The attempt of MBE growth of BP thin film is also described. After that, the fabrication procedures and electrical measurements of flexible BP devices for uniaxial bending strain are provided.

Chapter 4 – The result of the synthesized BP crystal is given. Raman spectroscopy of BP and polarized Raman response of BP are provided. Further characterization of the BP crystal quality is made by TEM. The high angle annular dark-field (HAADF) image, high resolution (HR) TEM image, energy dispersive X-ray (EDX), and selected area electron diffraction (SAED) pattern are given to ensure the excellent crystal quality of the synthesized crystal.

Chapter 5 – The growth attempts of MBE BP thin film is provided. Reasons for the failed attempts and characterization of the successful growth of BP thin film are given.

Chapter 6 – Electrical measurement analysis of flexible BP device. The drain-source current and drain-source voltage of the device is provided. The corresponding calculation and electrical conductance with and without strain is also analyzed.

Chapter 7 – The conclusion of the whole research is comprised. The achievement and

inadequacy of this study are listed. Possible future work of this study is suggested.

Chapter 2 Literature review

2.1 Background of Phosphorous Material

This section will give a background of phosphorus materials to understand their properties. As shown in Figure 2.1, there are various phosphorus allotropes such as BP, BlueP, diphosphorus, violet phosphorus (VP), RP, and WhiteP. Diphosphorus (P_2) is one of the allotropes of phosphorus in the gaseous form obtained through cracking WhiteP (P_4) at 1100 K [38].

BlueP is a relatively newly discovered type of phosphorus. It is a stable phase phosphorous material that was grown by MBE and experimentally studied by in-situ Scanning Tunneling Microscopy (STM) [29]–[32]. It has a constant 3.28 Å lattice constant in contrast to BP. WhiteP, also named yellow phosphorus, is the most toxic of allotropes [38]. It consists of tetrahedral P_4 molecules (Figure 2.1d). VP (Figure 2.1e) is annealed from RP over 550°C [38]. RP (Figure 2.1f) is formed by heating WhiteP to 250°C [38].

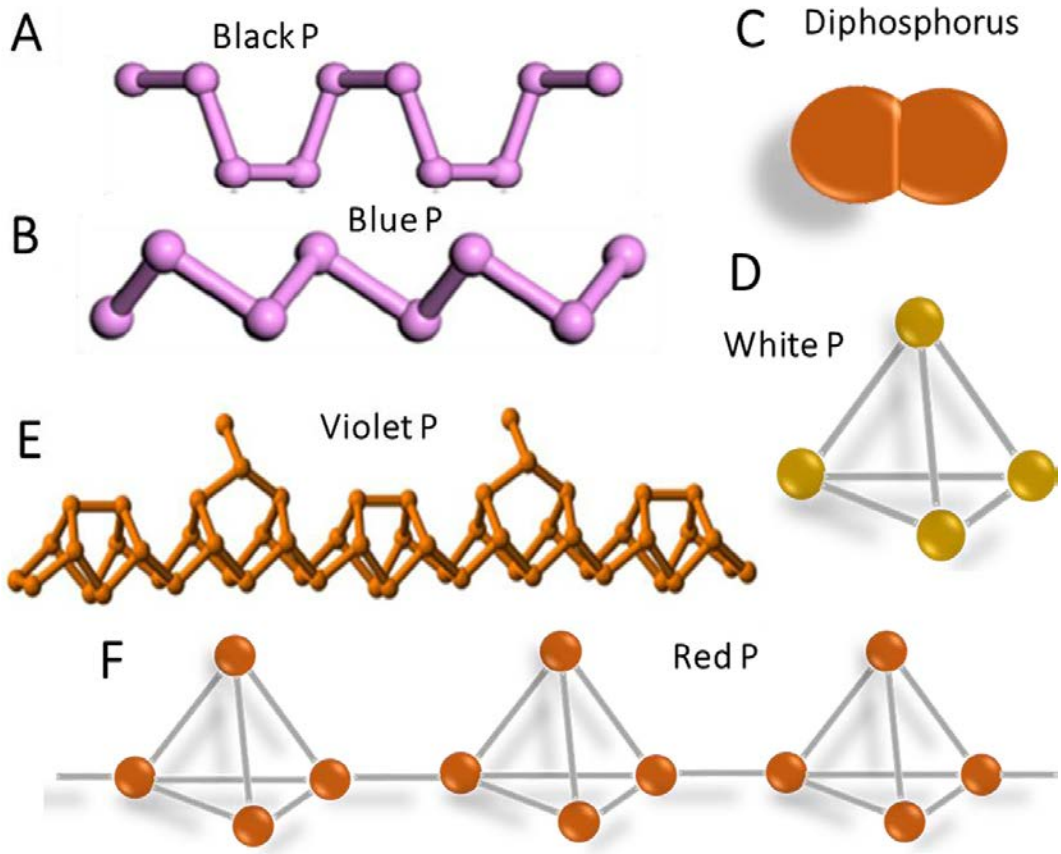

Figure 2.1(a-f) Allotropes of phosphorus. [38]

Among all the allotropes of phosphorus, BP is the most stable phase in ambient conditions [39]. BP has a layered structure similar to graphite, where adjacent atomic layers are stacked together through weak van der Waals force. It was found that the sp3 phosphorus atoms in a single layer are covalently bonded, and each atom is bonded to three neighbor atoms with one lone-electron pair due to the sp3 hybridization [40]. As a result, BP has a 'puckered honeycomb' structure [38], as shown in Figure 2.1a. It has an armchair and zigzag in-plane directions with lattice constants of 4.37 Å and 3.31 Å [41], respectively. The asymmetric unique A17 crystal structure of BP, shown in Figure 2.2,

creates a unique in-plane anisotropic property [42]. It was revealed that BP exhibits orthorhombic, rhombohedral and simple cubic phases [38] depending on the environmental pressure. In atmosphere pressure, BP exists in an orthorhombic crystal structure with five valence electrons in its outer shell [43]. The orthorhombic phase BP is converted to a rhombohedral phase at 5.5 GPa and a simple cubic phase at 10 Gpa [44]. This phase transition was reversible and independent of any temperature variation [45].

Due to the layered structure of BP and BlueP, they are the two phosphorus allotropes considered 2D materials. In addition, 2D BP and BlueP were also successfully prepared in various experiments.

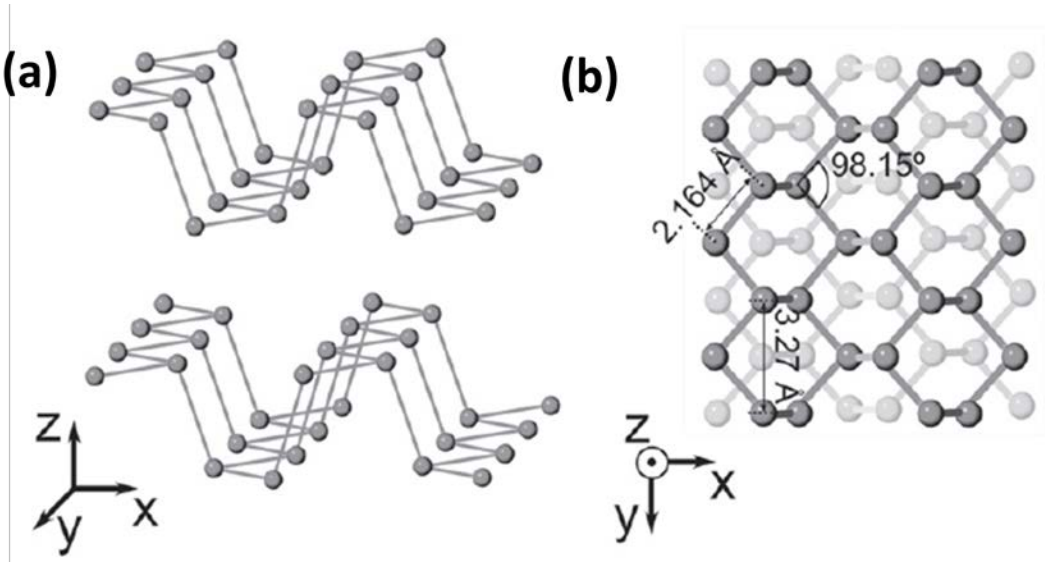

Figure 2.2 (a) Side view and **(b)** top view, of the A17 BP crystal structure.[42]

2.2 Optical Properties of Black Phosphorus

In order to fully understand the properties of BP, a tremendous amount of work has been carried out by many scientists. In this section, the optical properties of BP will be discussed. In addition, studies will be included about BP's bandgap, Raman spectroscopy, and anisotropy behavior.

BP is an exciting material with variable direct energy bandgap by tuning the number of layers. Figure 3a shows a theoretical band structure of bulk BP obtained by first-principle calculations with symmetry points stated in Figure 2.3c. It shows that bulk BP has a 0.3 eV direct energy bandgap [46]. The band structures of monolayer, bilayer and trilayer BP in Figure 2.3b indicates that BP has an increasing direct energy bandgap with decreasing thickness, while a 2.0 eV bandgap value can be achieved in monolayer BP [47]. These theoretical studies of the energy bandgap of BP were verified by optical absorption [48] and photoluminescence spectroscopy [10] experiments.

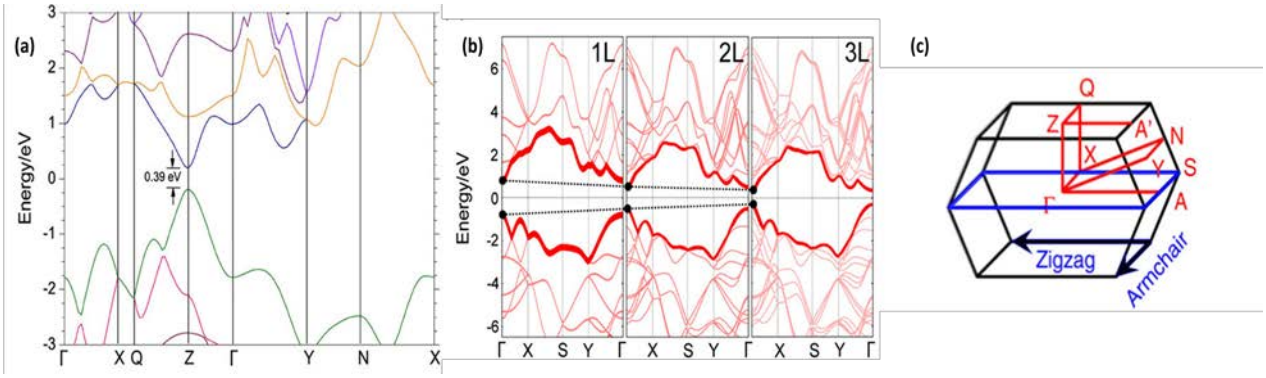

Figure 2.3 Calculated electronic band structures of **(a)** bulk BP and **(b)** monolayer, bilayer and trilayer BP, **(c)** first Brillouin zone of bulk BP.[12], [46], [47]

In Raman spectroscopy, BP normally has three Raman modes, A^1_g, A^2_g and B_{2g} modes, with 363 cm^{-1}, 470 cm^{-1} and 442 cm^{-1} [12], respectively (Figure 2.4b). Figure 2.4a summarises the Raman modes and the corresponding average wavenumber of BP. Jiang et al. [49] prove that the interlayer modes in BP are Raman-inactive as they are not at the center of the first Brillouin zone, unlike other 2D materials. When the incident laser beam is perpendicular to the sample surface, A^1_g, A^2_g and B_{2g} modes can be observed, as shown in Figure 2.4b. B_{1g} and B_{3g} modes are expected to exist only when the laser has a polarization along the axis orthogonal to the layer [12]. In addition, BP also has a Raman shift depending on its thickness. Figure 2.4c is an experimental result obtained by Phaneuf-L'Heureux et al. [50]. It displays the Raman shift towards a higher wavenumber with decreasing number of layers.

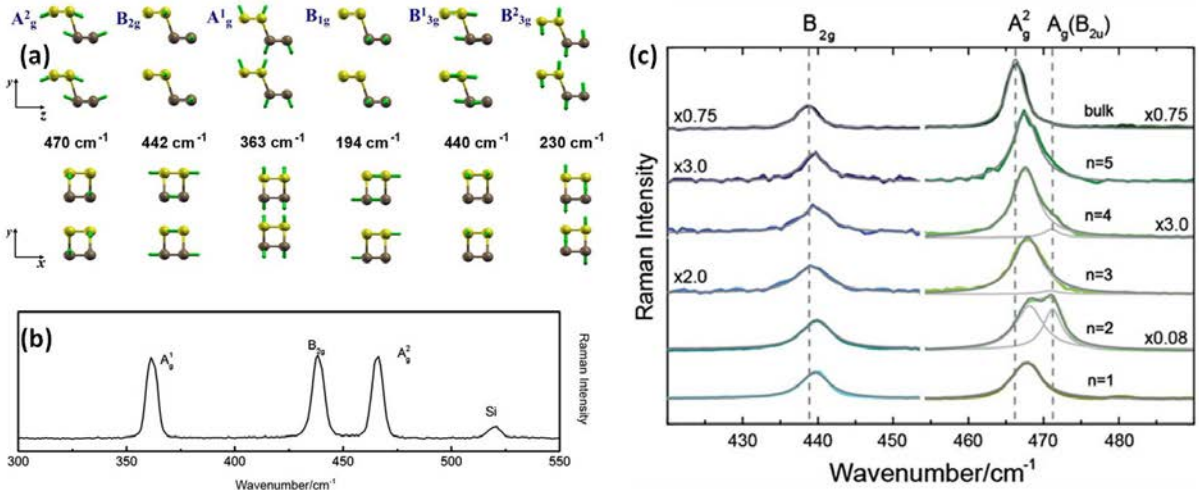

Figure 2.4 (a) Atomic displacement and wavenumber of each mode, **(b)** Raman spectrum of BP, and **(c)** Raman spectra of 1-5 layers BP. [12], [50]

BP also has an angular dependence of the Raman modes. As BP has ZZ and AC directions, as mentioned in chapter 2.1, this special crystal structure contributes to the anisotropy of the Raman intensity. Kim et al. [51] used a 632.8 nm laser with fixed incident polarization and rotating sample to obtain the angular dependence, as shown in Figure 2.5. Figure 2.5 shows that the intensity is dependent on the incident polarization.

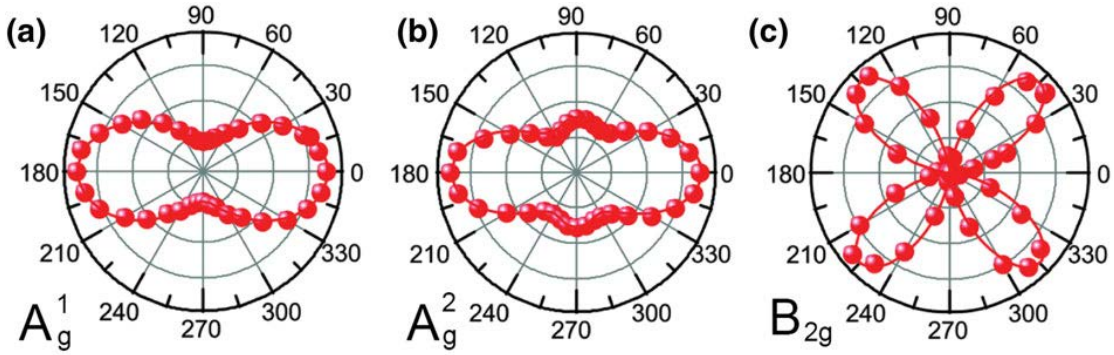

Figure 2.5 Angular dependence of **(a)** A^1_g, **(b)** A^2_g, and **(c)** B_{2g} modes in BP. [51]

2.3 Strain Induced Anisotropy

Numerous studies have been focusing on the anisotropy behavior of BP; some specifically analyzed the anisotropy of BP under applied strain. For example, Li *et al.* [36] suggest a redshift in Raman modes if a uniaxial tensile strain is applied on BP. Figures 2.6a and b illustrate the Raman shift of BP under the ZZ and AC strain, respectively. Atomic displacement of B2g mode is more sensitive to the ZZ strain, while both B_{2g} and A2g shows modest effect due to AC strain. Moreover, A_{1g} mode has almost no effect from the AC strain demonstrated in Figure 2.6b.

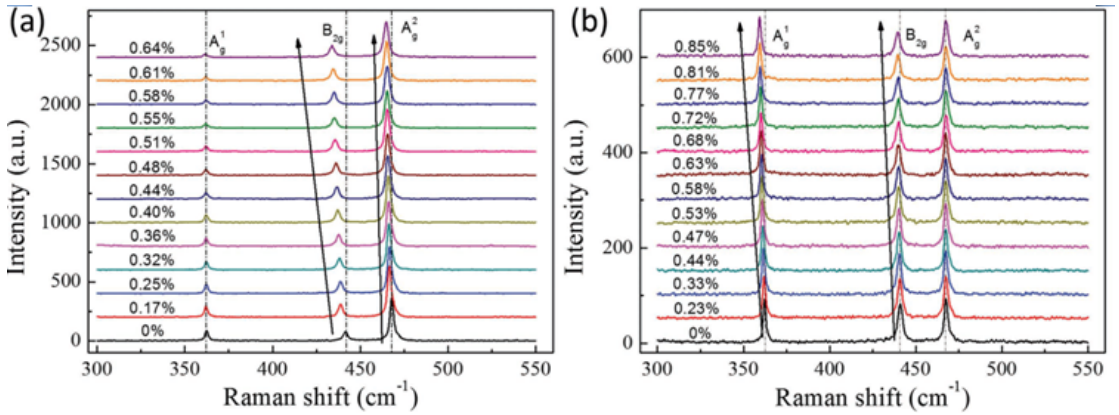

Figure 2.6 BP Raman Shift under uniaxial tensile strain in the **(a)** ZZ direction and **(b)** AC direction.[36]

Fei and Yang [37] then provided a theory that the electrical preference in BP can be changed with the appearance of uniaxial bending strain in the ZZ direction or biaxial bending strain of BP according to their DFT/PBE simulations. The switch of electrical preference in AC and ZZ directions is shown in Figure 2.7. The electrical mobilities of BP with 4K temperature and room temperature under biaxial strain and ZZ direction

strain are illustrated, respectively. The critical transition of anisotropic mobilities in BP occurs when the applied biaxial strain is greater than 3% (Figures 2.7a and 2.7c), or the applied uniaxial bending strain in ZZ direction is above 5% (Figures 2.7b and 2.7d). They stated that this transition is due to the switch in energy order of the first two conduction bands with strain applied in the ZZ direction (Figure 2.8), which cannot be seen in applying strain in the AC direction. Yet, this theory has not been proven experimentally.

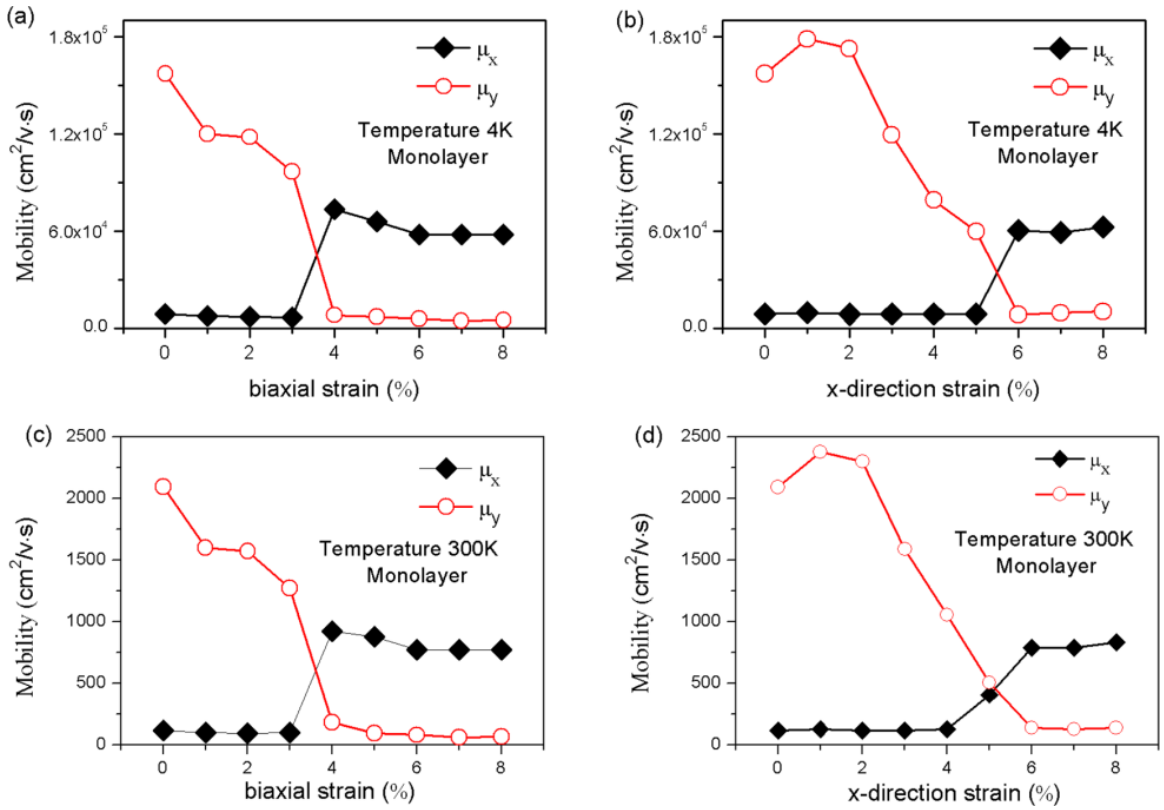

Figure 2.7 Electron mobilities of monolayer BP along the ZZ and AC directions for biaxial strain and uniaxial ZZ strain at (a,b) 4K temperature and (c,d) room temperature. [37]

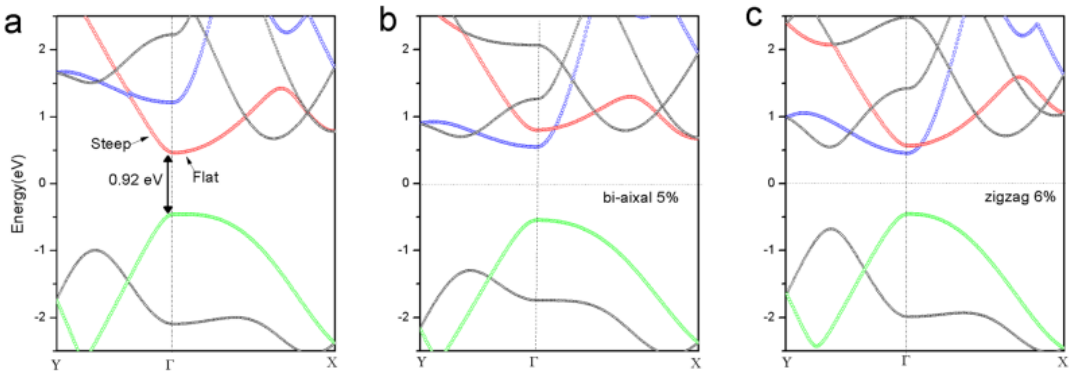

Figure 2.8 Band structures of (a) intrinsic monolayer phosphorene, (b) phosphorene with a 5% biaxial strain, and (c) phosphorene with a 6% zigzag uniaxial strain. [37]

2.4 Synthesis of Black Phosphorus

Since the discovery of BP, many synthesis methods have been utilized. It was understood that BP should not be available in nature, so scientists first synthesized BP by high-pressure routes from WhiteP or RP. Different approaches were developed afterwards, such as mechanical milling and bismuth-flux. However, the methods mentioned above are of a low potential for industrial applications due to their low throughput, high toxicity or poor economic effectiveness. Recently, a low-pressure route was discovered using a mineralization approach. In this research, a low-pressure route was applied to synthesize BP crystals.

High-pressure route

It was first suggested by Bridgman [11] in 1914, a 1.2 GPa high pressure and 473 K high temperature were used in the experiment to produce BP crystal. Many experiments were

carried out by using this method. For example, Robert [52] used a similar method with adjusted temperature and pressure to obtain a high crystallinity BP crystal. Li et al. [53] successfully used the high-pressure route to synthesize BP for field-effect transistor testing. This approach produces BP with high crystallinity. However, there are various concerns about this synthesis route. It is hazardous to continuously use high pressure and temperature, not to mention the difficulty of owning both the high pressure and high-temperature equipment. The high pressure and temperature system cannot produce BP crystals continuously, so this method is effective in making BP crystals but lacks practicality, unfortunately.

Mechanical milling

Suryanarayana et al. [54] invented two-type ball milling apparatuses to prepare BP powder from RP, including a mixer mill and a planetary ball mill. These methods are fast synthesis route, but the BP powder has relatively low crystallinity and an oxidation problem. Therefore, an upgraded system was used by filling the system with argon gas and putting the RP powder into stainless steel pot with stainless steel balls [54] to cure the oxidation of the BP resultant. However, the crystallinity was still relatively low and quickly varied with different mill apparatuses.

Bismuth-flux

Brown and Rundqvist [16] used liquid bismuth to produce BP, namely the bismuth-flux method. BP single crystals were grown from the WhiteP solution in the liquid bismuth, and the experiment was conducted in a vacuum condition. However, the WhiteP used was relatively low purity since pure WhiteP is highly reactive and inflammable. Therefore, sulfur and selenium impurities were found and difficult to remove from the BP product. Adjustment with using RP over WhiteP [16] was made, but RP does not dissolve in liquid bismuth, increasing the complexity of the synthesis. However, this method has the advantages of an efficient conversion process and is easy to control. The drawbacks are using poisonous WhiteP and a large amount of costly bismuth metal.

Low-pressure route

None of those mentioned above methods is practicable in industrial applications due to their low throughput, high toxicity or non-economic workup procedures. Recently, a surprisingly low-pressure route to growing BP was reported. It used a mineralizer as a reaction promoter, which allowed the production of high-quality phosphorus at non-toxic conditions. The transformation of RP into BP can be realized via SnI_4 mineralization [17]. The whole transformation took place without a temperature gradient, and the crystals grew 1 - 2 mm in diameter within 10 days. Similarly, AuSn was used as the starting material, and SnI_4 mineralizer with RP was applied to produce BP [55]. A 1.5 cm

diameter BP crystal was made within 32.5 h.

Another low-pressure route used tin and iodine as the catalysts with RP to produce micro ribbon BP with high crystallinity by CVT [56]. BP crystal and residue tin iodide were obtained in the experiment. The residue can be easily cleaned by acetone, methanol and isopropyl alcohol (IPA). In this research, this mineralization synthesis method of BP was employed to grow high purity BP crystal as well as the solid source for MBE growth.

2.5 Fabrication methods of Two-Dimensional Black Phosphorus

In 2014, the first exfoliation of BP was successfully made [10]. There has been an increasing amount of work focusing on preparing 2D BP since then. 2D BP is crucial for exploring the structural and physicochemical properties of BP. Therefore, to explore the potential applications of BP, 2D studies of BP were necessary. To date, many efforts have been dedicated to developing different ways to fabricate 2D BP. The fabrication methods can be divided into two main categories – the top-down approach and the bottom-up approach. Figure 2.8 lists the most known 2D BP preparation methods.

Mechanical exfoliation

Mechanical exfoliation is a traditional top-down approach to fabricating 2D materials. In 1990, Seibert et al. [57] exfoliated graphite film with transparent tape. In 2004,

Novoselov et al. [1] exfoliated single-layer graphene with scotch tape. For mechanical exfoliation, the energy required to remove a layer from the adjacent layer is quantified by the surface energy [58]. The weak van der Waals bond can be broken with adequate energy and produce a 2D form of the material. According to the multilevel quantum-chemical calculations, the exfoliation energy of BP was -151 meV per atom [59]. Adhesive tape exfoliation of BP was also successfully obtained [58], [59]. The tape was used to peel BP off from the bulk, a few layers of BP adhered onto the tape, and subsequent peeling from the tape can further reduce the thickness of the exfoliated BP. The peeled BP can be put onto a substrate, followed by cleaning it with acetone, methanol, IPA to remove residue of the tape. This approach only applies a shear force to the bulk crystal; no chemical reaction was included. Therefore, the crystal structure and the crystal quality of the BP flake can be primarily maintained as the bulk. It is fast, cost-effective and straightforward; most importantly, it is beneficial for fundamental studies of BP.

Sonication assisted liquid-phase exfoliation

Liquid phase exfoliation requires a suitable solvent to fabricate 2D BP successfully. A three-step exfoliation approach can be considered [60] – immersion into a solvent, ultrasonication, and purification. 2D BP has a surface tension of 35 - 40 mJm^{-2}

determined by optical absorption spectroscopy [19]. A solvent with similar surface tension can maximize the exfoliation rate. *N*-methyl-2-pyrrolidone(NMP) [20], *N*-cyclohexyl-2-pyrrolidone (CHP) [21], dimethylformamide (DMF) [22], dimethyl sulfoxide [60], and acetone [23] were used for liquid-phase exfoliation of 2D BP. The ultrasonication process breaks the van der Waals bonding between layers while not influencing the covalent intralayer bonding. After the ultrasonication, the resultant solution is purified by centrifugation to yield 2D nanoflakes. The ultrasonication time and centrifugation rate are important parameters for yielding high-quality 2D nanoflakes [61]. This method is useful for massive production, but the lateral dimensions of the flakes are small, and monolayer can be hardly obtained.

Electrochemical exfoliation

Electrochemical exfoliation is based on anodic oxidation or cationic intercalation [60]. BP was used as an electrode immersed in a conductive solution electrolyte. The generated current would deform the layered BP by applying voltage. Operating voltage and a good selection of electrolytes are the prerequisites for a good electrochemical exfoliation. Na_2SO_4 or H_2SO_4 with BP anode and Pt cathode [24] were used to fabricate 2D BP. However, the anodic oxidation leads to partial oxidization of BP. A cationic intercalation approach was produced to eliminate this problem. The BP was used as cathode instead,

whereas Pt was used as anode [25]. The electrochemical exfoliation method is more facile, faster, and more environmentally friendly than liquid-phase exfoliation. In addition, this exfoliation technique can be easily controlled by the applied potential.

Other bottom-up methods

Bottom-up fabrication was widely used in many 2D materials, such as h-BN and TMDs. CVD is a common bottom-up approach that involves using volatile precursors at high temperatures to react and decompose on the substrate surface to produce 2D materials. However, there are limited studies on CVD growth BP. Therefore, an in-situ CVD-type approach was used for growing 2D BP directly on the silicon substrate. Another PLD technique method to produce BP ultrathin films was also demonstrated. Detail will be provided in sections 2.8.

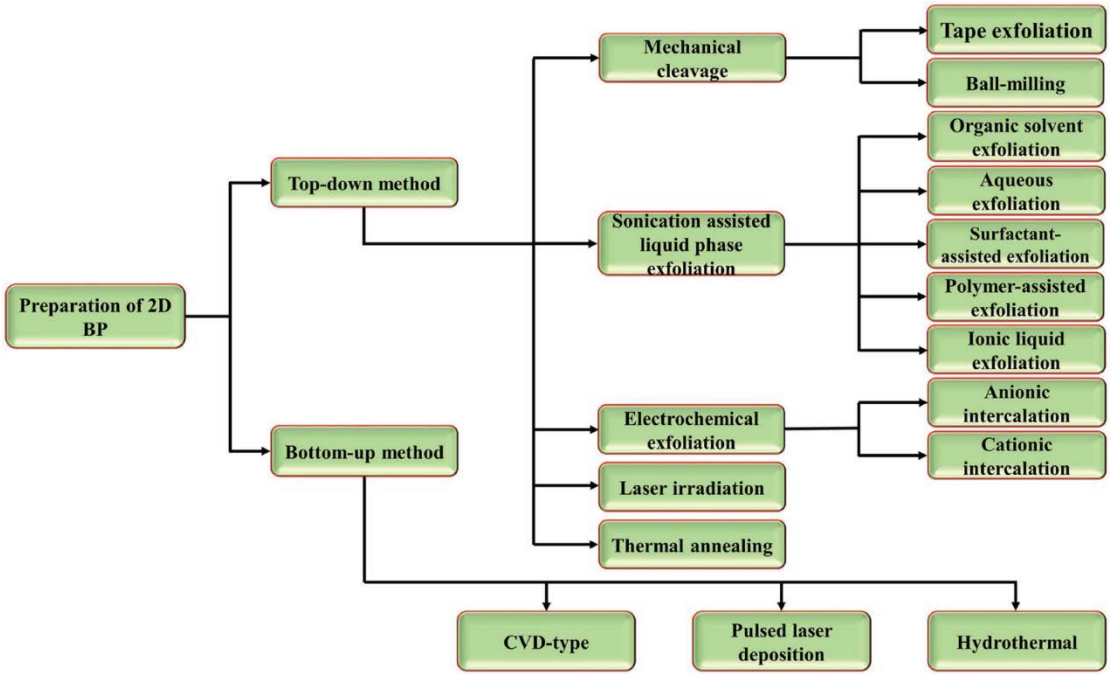

Figure 2.9 Available 2D BP fabrication methods.[61]

Although there are various fabrication techniques for the growth of 2D BP, no perfect method was developed. Figure 2.9 compares the growth BP by six approaches in five categories – duration, yield, crystal quality, lateral dimension, and scalability [60]. There is a tradeoff between those five critical factors of growing 2D BP in all the fabrication methods. As a result, a new and better way for 2D BP growth can benefit.

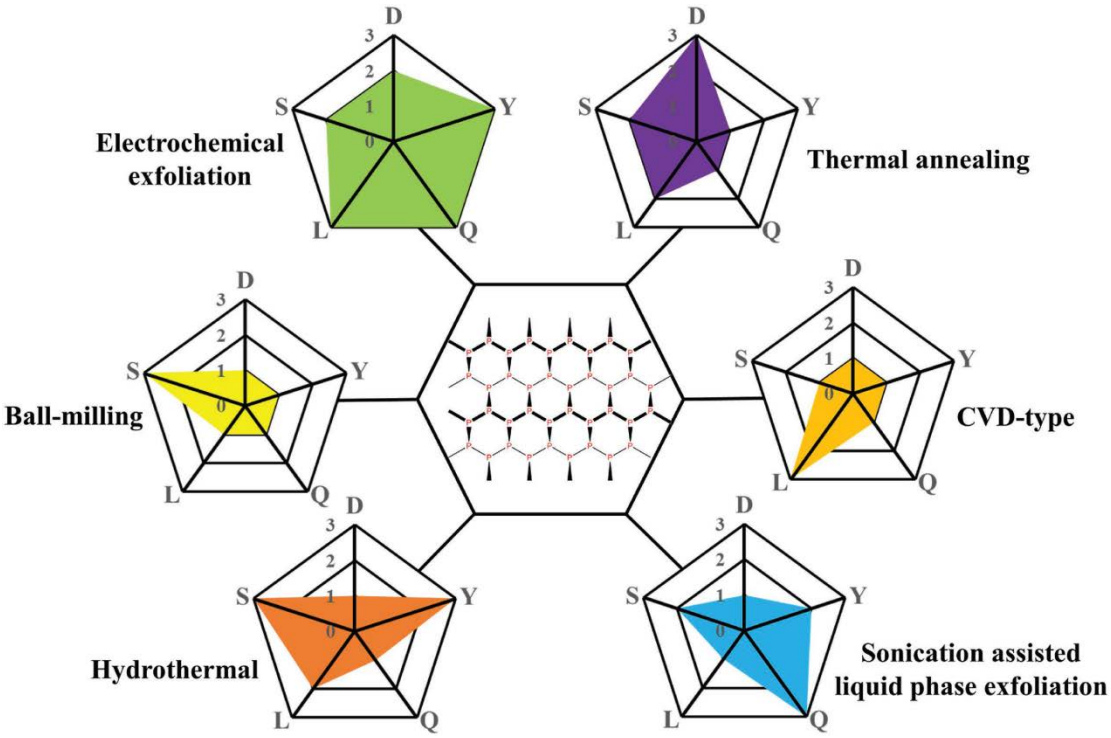

Figure 2.10 Comparison of six 2D BP fabrication strategies by evaluating the duration of grown 2D BP (D), yield (Y), BP quality (Q), lateral dimensions (L) and scalability (S). For D, 1 = high, 2 = moderate, and 3 = low. For Y, Q, L, and S, 1 = low, 2 = moderate, and 3 = high.[60]

2.6 Instability of Black Phosphorus

Bulk BP is stable at atmospheric conditions for a few months long but exfoliated BP shows a relatively high reactivity and air instability [39]. Figures 2.10a-d show the AFM images of the mechanical exfoliated five-layer BP flake when exposed to ambient conditions. The BP flake was expanded in volume non-uniformly and disappeared within 100 hours [62]. The thinner BP flake absorbs water faster and degrades at a faster rate. Figure 2.10e and 2.10f show the physical changes in height and volume of the BP flake [62], in ambient conditions, respectively. There is also a chemical change of BP towards a liquid phase and eventually disappears on the surface.

Figure 2.11 is the experimental evaluation of BP degradation on either humidity or light [63]. The image was mapped from the Raman intensity over eight days of observation. Figure 2.11b shows that humidity reduces the overall profile of the BP flake, and Figure 2.11c shows that light reduces the lateral dimensions of the flake. It was suggested that light is the main factor governing the degradation and photo-oxidation originating at the edges of the BP flake [63]. Oxygen ion was generated on BP under ambient light and dissociated on the BP surface to form P-O bonds. The water molecules in the air eventually drew the bonded P_xO_y out of the surface to remove P from the flake. The chemical reaction is stated below:

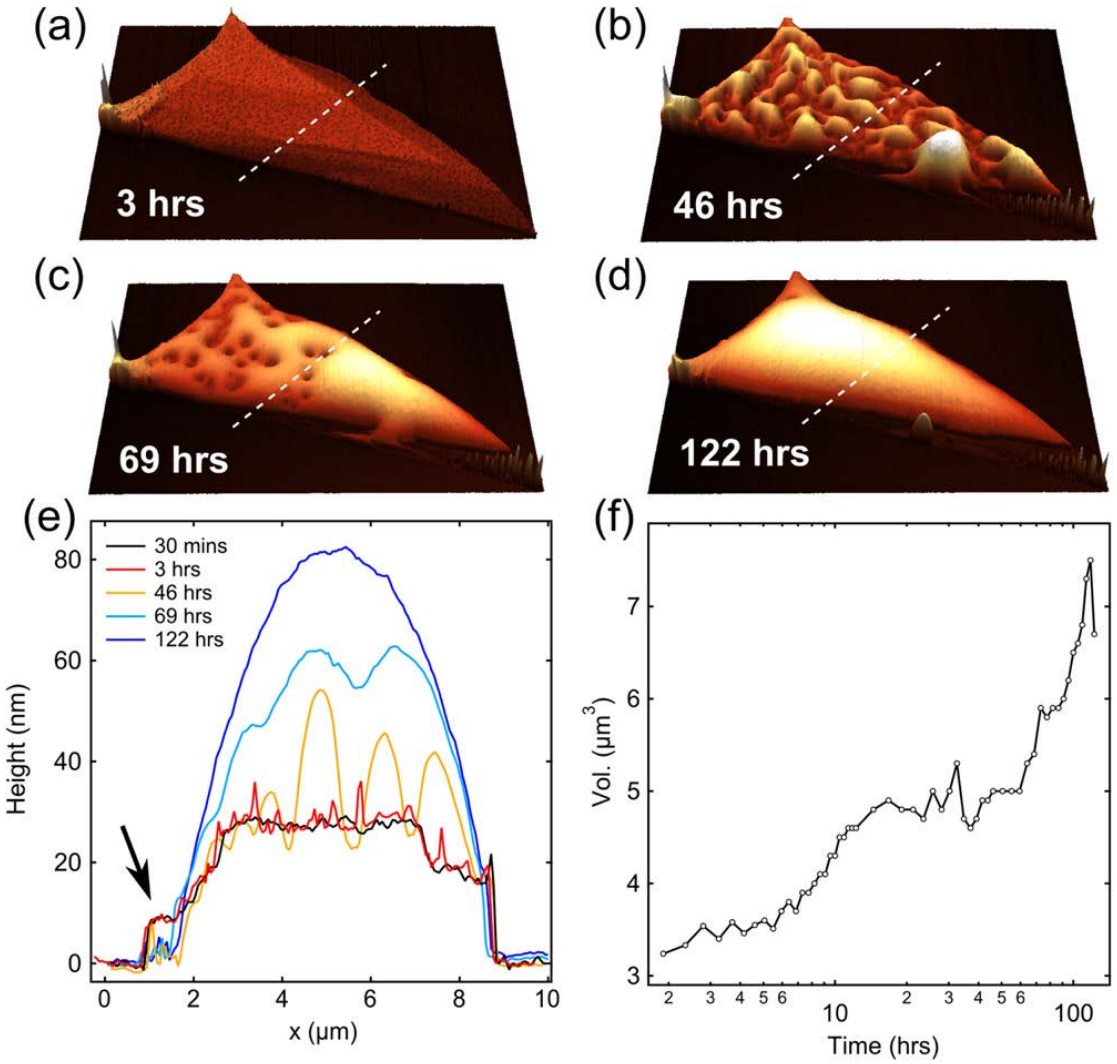

Figure 2.11 (a-d) AFM images of BP flake in air at 3, 46, 69 and 122 hours after exfoliation, **(e)** AFM height profile of the degraded BP, **(f)** total volume of BP and water over the degradation period.[62]

$$O_2 + hv \xrightarrow{2D\ BP} O_2^- + h^+ \qquad \text{Equation 2.1}$$

$$O_2^- + 2DBP + h^+ \rightarrow P_xO_y \qquad \text{Equation 2.2}$$

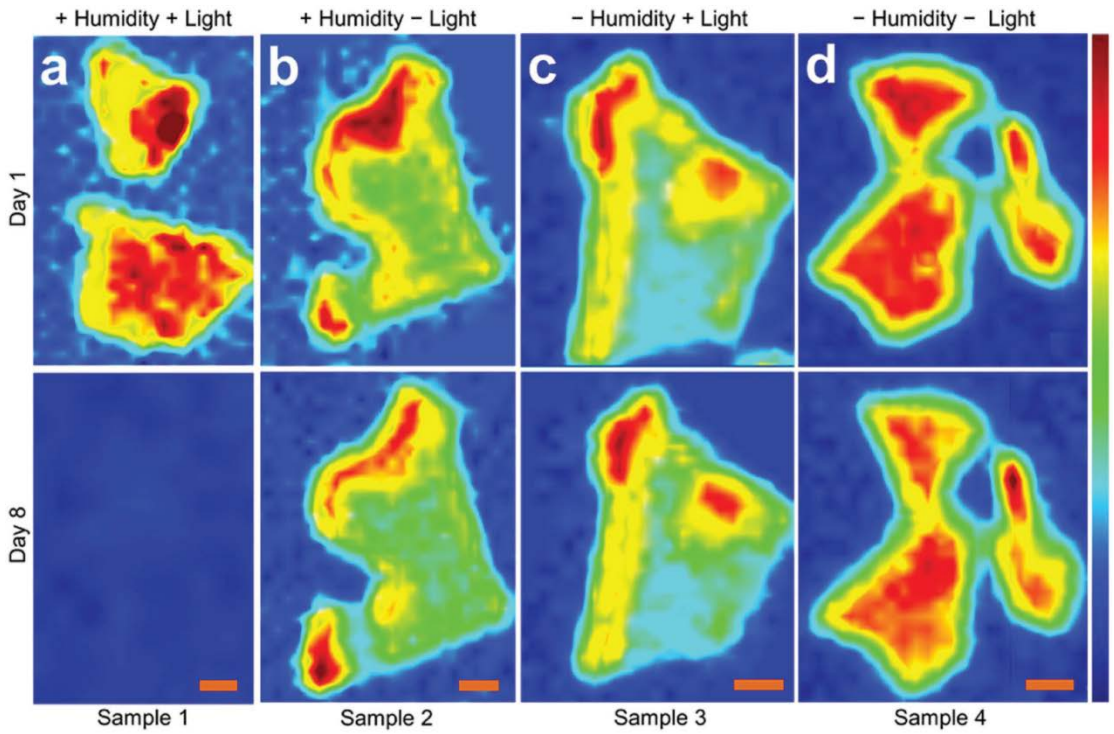

Figure 2.12 Spatial maps of Raman intensities change under **(a)** ambient environment, **(b)** absence of light, **(c)** absence of humidity, **(d)** absence of humidity and light.[63]

2.7 Molecular Beam Epitaxy Growth of Blue Phosphorus

MBE is a state-of-the-art epitaxial growth method of 2D material. BP was used as a solid source in the MBE to grow BlueP [29]–[32]. These studies are worth referring to since they provide evidence that MBE growth of phosphorus material is possible.

Zhang et al. [29] used Au (111) substrate prepared by Ar+ bombardment (1.5 kV, 1×10^{-5} mbar) and subsequent annealing at 500 °C to grow single layer BlueP. Figure 2.12a is an in-situ STM image of a 3 min deposition of BP source at 260 °C with subsequent annealing at 150 °C for 60 min. Phosphorus clusters were produced but with very low yield. The annealing temperature was increased to 250 °C to obtain a well-defined monolayer of BlueP with a small domain size (Figure2.12b). Another trial based on heating the Au (111) substrate for 20 min at 230°C rather than room temperature created a well defined hexagonal BlueP structure with a larger domain size (Figure 2.12c).

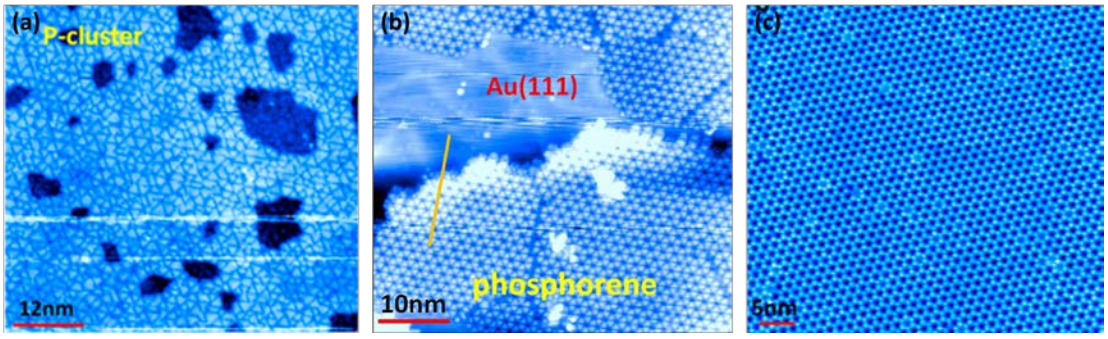

Figure 2.13 Close-up in-situ STM images of **(a)** 3min deposition of BP source at 260 °C with 150 °C annealing on Au (111), **(b)** 3 min deposition of BP source at 260 °C with 250 °C annealing on Au (111), **(c)** 20 min deposition with 230 °C on Au (111).[29]

Gu et al. [30] used Cu(111) and Au(111) substrates prepared by repeated Ar+ bombardment (1.5 kV, 6×10^{-5} mbar) and subsequent annealing at about 500 °C to grow quasi-free-standing single layer BlueP. The BP source was heated at 290 °C, and the substrate temperature was kept at 250 °C for both Cu (111) and Au (111). Only phosphorus clusters were observed on top of Cu (111) in their experiment, as shown in Figure 2.13a. Hexagonal structure BlueP was grown on Au (111) (Figure2.13b).

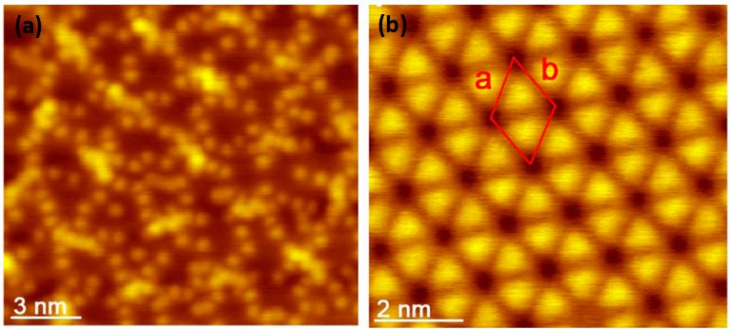

Figure 2.14 Close-up in-situ STM images of **(a)** 290 °C BP deposition on 250 °C Cu (111), **(b)** 290 °C BP deposition on 250 °C Au (111).[30]

Similar approaches were made by using Au (111) substrate at 260°C [31] and using InP source instead of BP source [32]. Again, the results were in agreement with the above experiments. Therefore, the ultra-high vacuum MBE growth of phosphorus was proven to be possible.

A computational study done by Zhu and Tománek [64] evidenced that the preferential phase of phosphorus should be determined by the lattice constant and the symmetry of the substrate. They suggested that hexagonal symmetry with a reasonable lattice constant,

such as MoS_2, Zr(0001) and Sc(0001), are preferable for BlueP growth, whereas rectangular lattice substrates are favored for BP growth.

2.8 Black Phosphorus Synthesis by Pulsed Laser Deposition

Yang and his group[27] discovered a new and unique approach to produce amorphous BP on SiO_2 substrate with a low temperature and low-pressure PLD in 2015. BP cluster formation can be achieved by the high-density plasma provided in PLD. Figure 2.14 shows the results obtained by Yang[27]. The EDX and XRD spectra show a high content of P with observable BP orthorhombic structure. However, the BP thin films grown by PLD was amorphous according to the SAED image and the board full width at half maximum (FWHM) of the Raman modes. Figure 2.14e also compares the Raman peaks of PLD BPs grown at various temperatures; noticeably, a-BP Raman peaks can only be observed distinctively at 150 ^{o}C substrate temperature on SiO_2 substrate.

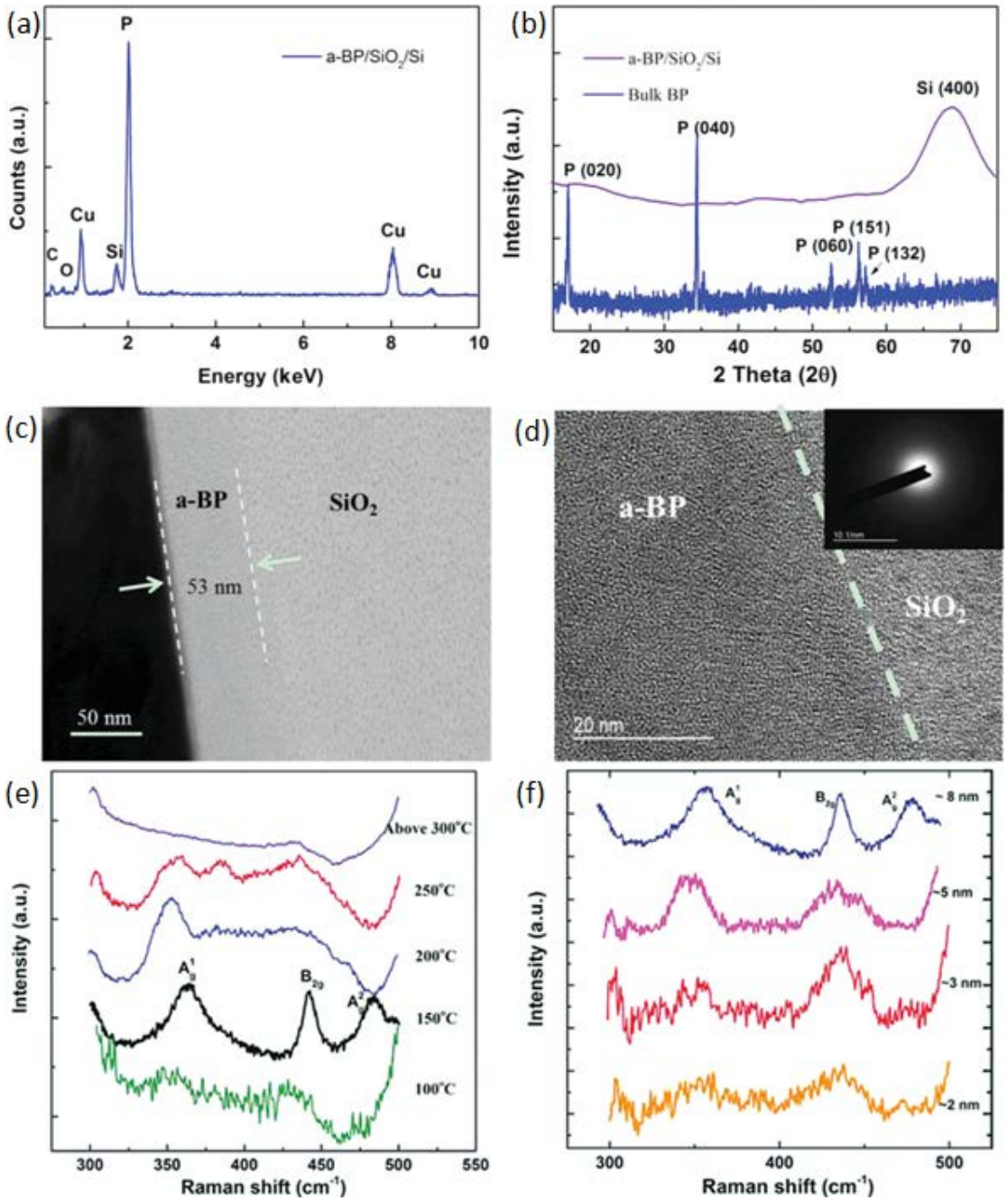

Figure 2.15 **(a)** EDX spectrum, **(b)** XRD patterns, **(c)** cross-sectional TEM image, **(d)** HRTEM image (inset: SAED pattern), **(e)** Raman modes at different substrate temperatures, and **(f)** Raman response at different thickness, of a-BP produced by PLD.[27]

Few layers of polycrystalline BP was later achieved by the PLD with rapid dry N_2 gas cooling[28]. Mica substrate was used instead of SiO_2 here. The grown BP's Raman peaks

shown in Figure 2.15a have a more narrow FWHM than reported previous a-BP [27] . The BP atomic structure and purity can be seen in Figures 2.15b and c. On top of that, the SAED image illustrated in Figure 2.16d shows a polycrystalline pattern. Thus, these studies proposed that BP can be synthesized by low temperature and low-pressure routes instead of the traditionally high pressure and high-temperature methods.

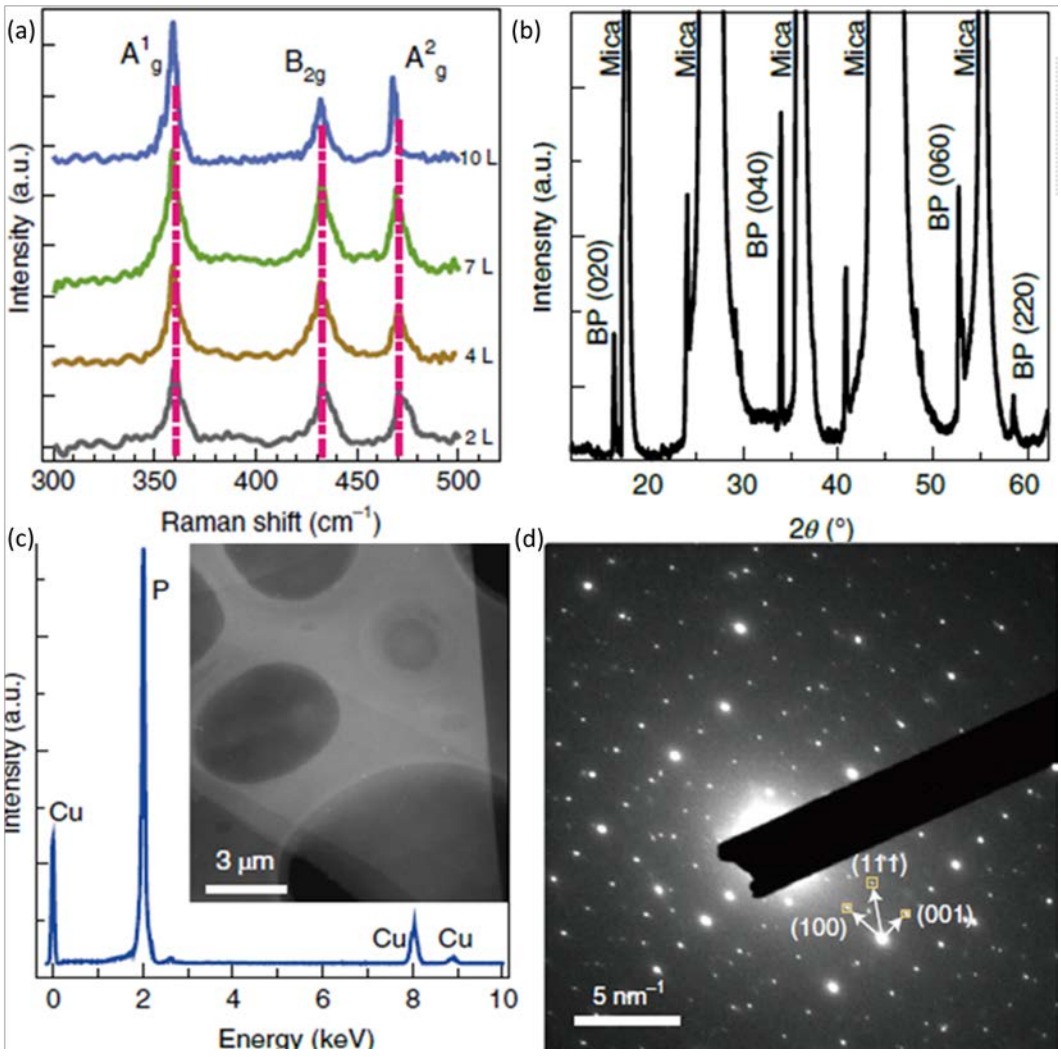

Figure 2.16 (a) Raman spectra on few-layer BP, **(b)** XRD spectrum, **(c)** EDX spectrum, and **(d)** SAED pattern, of the PLD grown polycrystalline BP on mica substrate.[28]

Chapter 3 Experimental and Characterization Methods

3.1 Synthesis and Characterization of Black Phosphorus Single Crystal

3.1.1 Chemical Vapor Transportation

CVT is a technique in which the volatilized precursor materials and transport agents are sealed in an ampoule and transported from one end to the other to form single crystals by a temperature gradient [56]. Various single crystals of TMDs [65], [66] and BP [17], [55], [56] were obtained by this method.

Figure 3.1 demonstrates the process of CVT, where a quartz tube is placed inside the furnace with one end closer to the centre of the heater to create a temperature gradient. The precursors were weighted and put into a quartz tube (13mm inner diameter, 1mm wall thickness) in this experiment. Then the tube was evacuated and sealed with a 110 mm in length by a vacuum sealing tool. The precursors were composed of 20 mg of Iodine (I2, 99.8% of purity, ACS reagent), 30 mg of Tin (Sn, 99.995% of purity) and 400mg of Red Phosphorus (RP, ≥97% of purity). Tin and iodine were used in a chemical reaction to transform RP to BP at high temperatures, as claimed in reference [56]. The

furnace temperature was programmed in the previous research, as shown in Figure 3.2. Slow temperature drop after 600 °C ensured sufficient time for the gaseous phosphorus to crystallize [18]. BP single crystals were formed on the other end of the tube shown in Figure 3.1. The produced BP crystals were separated from the waste and washed by ultrasonication in acetone for 10 minutes and IPA for 10 minutes. They were kept in the vacuum container until use.

Figure 3.1 Schematic diagram of CVT.[67]

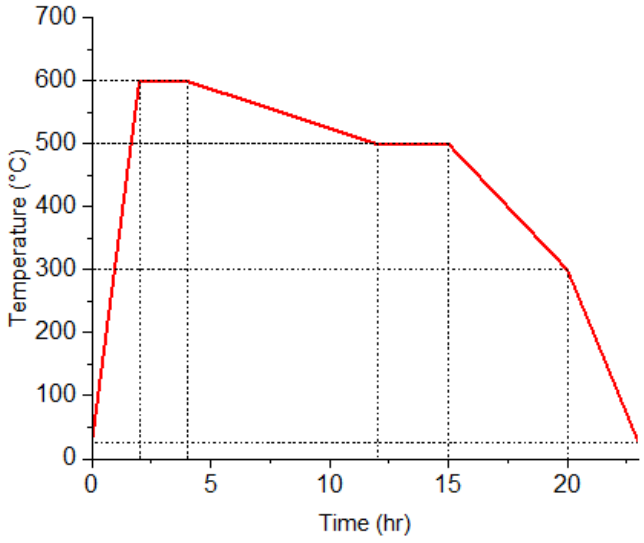

Figure 3.2 Furnace temperature process for CVT.

3.1.2 Raman spectroscopy

Raman spectroscopy was then employed to confirm the identity of the grown single crystals. It is based on the Raman scattering of a monochromatic light where the light interacts with molecular vibrations, phonons or other excitations in the system to produce a shift up or shift down in energy, as described in Figure 3.3 [68]. The Raman shift can be explained by the energy difference given in the following equation:

$$E = \hbar(\omega s - \omega 0) \qquad \text{Equation 3.1}$$

where E is the energy difference between incident and scattered photons, $\hbar$ is the reduced Planck constant, ωs is the scattered photon frequency, $\omega 0$ is the incident photon frequency.

The energy of the incident photon can be equal, larger, or smaller than the scattered photon. Rayleigh scattering means the energy of photon after scattering remains. As shown in Figure 3.3, the energy difference when the scattered photon has lower energy than the incident photon is called Stokes scattering. Oppositely, it is named Anti-Stokes scattering when the scattered photon has higher energy than the incident photon.

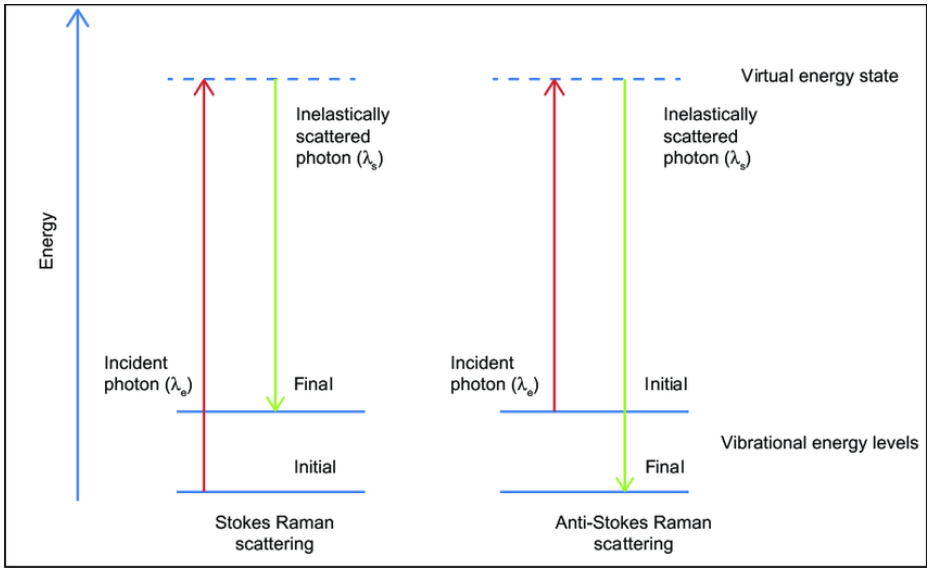

Figure 3.3 Stoke shift and anti-stoke shift in Raman spectroscopy.[68]

A Witec alpha 300R Confocal Raman imaging microscope system was employed. A 532 nm green laser with a power of 0.5 mW was used, the spot size was focused to below 1 μm in the measurement. The synthesized crystal was carried to the Raman system to confirm its Raman peaks in bulk form and exfoliated form. Afterwards, the polarized Raman spectroscopy was also implemented to check the zigzag and armchair directions of the BP flakes to prepare flexible BP device fabrication.

3.1.3 Transmission Electron Microscopy

TEM uses a transmission of an accelerated electron beam in a high vacuum column to project the diffracted electron pattern of the sample[69]. Focused electrons are subjected to the sample surface on the carbon copper grid through the electromagnetic lens. The diffracted pattern through the sample indicates the crystal structure and atomic size. JEOL

JEM-2100F Scanning Transmission Electron Microscopy (STEM) was used. The observation was conducted with controlled sub-200keV electron energy. The HAADF image, HR image, SAED, and EDX of the synthesized BP crystal was taken and analyzed. Flesh BP was transferred to the carbon copper grid. Standard mechanical exfoliation was followed by a Revalpha thermal release tape transfer. The exfoliated BP on the scotch tape was transferred to the thermal release tape. It was then put on top of the grid and heated to 140^{o}C for a few seconds. The prepared TEM specimen was directly transferred into the TEM system for examination.

3.2 Synthesis and Characterization of 2D Black Phosphorus

3.2.1 Molecular Beam Epitaxy

The principle of MBE is to heat up the solid source material and break it down to atoms or clusters of atoms so they can migrate and lie onto the substrate, slowly diffusing over the substrate surface [70]. It offers a great atomic precision of the thin film and enables large scale fabrication with good uniformity. Figure 3.4 is a configuration of the MBE system where the source material used in this experiment was put into the effusion cell.

In this study, the MBE growth of BP was attempted by various conditions summarized by Table 3.1. BP and GaP were used as the source materials. SiO_2, Al_2O_3, and mica were the substrates. SiO_2 and Al_2O_3 substrtates were tested since they have amorphous structural

surface which could be benefetial to the growth of unqiue orthorhombic BP. In addition, the mica susbstrate was chosen for comparison to the previous PLD gorwn BP work [28]. The source temperature of BP and GaP was tested and monitored by the quartz crystal microbalance. The base pressure was ensured to be below $5x10^{-8}$Torr. Different substrates, source temperature, substrate temperature, and growth time were tested. The quartz crystal microbalance monitored the growth rate. In addition, the sample was quickly transferred to the load lock after growth to reduce the excess heat in the natural cooling process that could attribute to the deterioration of the crystalline BP[28].

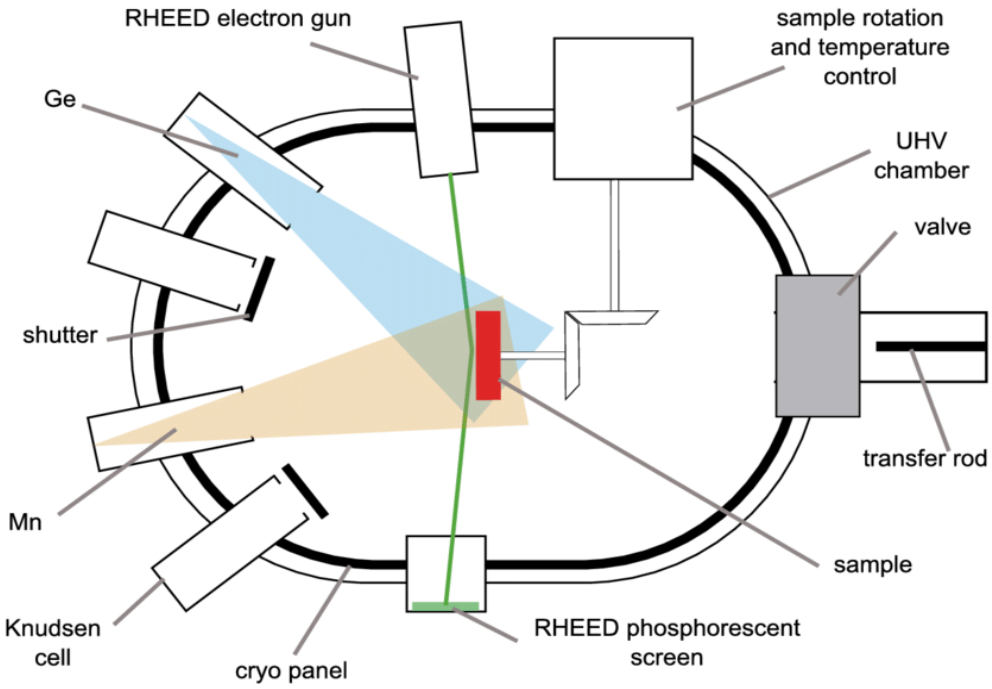

Figure 3.4 MBE configuration.[70]

Table 3.1 Experimental conditions for the MBE growth of BP

Source Material	Substrate	Substrate temperature (°C)	Source temperature (°C)	Base Pressure (Torr)	Growth time (min)
BP	SiO_2	Room Temp.	260	3×10^{-8}	180
		100	290	5×10^{-8}	180
		150	290	5×10^{-8}	180
	Al_2O_3	Room Temp.	260	3×10^{-8}	180
		100	320	5×10^{-8}	180
		150	320	5×10^{-8}	180
GaP	SiO_2	Room Temp.	870	5×10^{-8}	60
		160	870	5×10^{-8}	60
	mica	300	870	5×10^{-8}	60

3.2.2 X-ray Diffraction

XRD characterizes the crystal structure according to Bragg's diffraction equation. It can be used to determine the crystal structure, phases, and lattice planes[71].

$$2d\sin\theta = n\lambda \qquad \text{Equation 3.9}$$

where d is the interplanar spacing, θ is the diffraction angle, n is any positive integer, and λ is the wavelength of the X-ray.

In this experiment, Rigaku SmartLab X-Ray Diffractometer with the CuKα X-ray of 0.154 nm wavelength was used to characterize the thin film grown by MBE.

3.2.3 Atomic Force Microscopy

AFM uses a flexible cantilever with a sharp tip to scan the sample surface. The interaction force between the tip and the sample surface will be kept constant, so the cantilever will bend according to the change in sample thickness[72]. The electrical potential of each point is measured and plotted after the scan of the whole sample surface to create a mapping AFM image and surface roughness profile. AFM (Bruker Nanoscope 8) surface scanning was performed to determine the surface morphology of the growth BP thin film by MBE.

3.3 Fabrication and electrical measurement of flexible black phosphorus device

3.3.1 Fabrication procedures

Flexible Kapton polyimide (PI) substrate was used in this experiment. Marking was first patterned on the PI film by photolithography using SUSS MA6 Mask Aligner. Photoresist AZ5214E was spun at 500 rpm for 5s and 4000 rpm for 60s, and baked at 105 ^{o}C for 180s. The film was patterned by 350W ultraviolet lamp exposure for 10s and developed by AZ300MIF developer. E-beam Evaporation deposited 5nm/50nm of Cr/Au. The residue photoresist was lifted-off by acetone and cleaned by IPA.

After the marking pattern was layered, the BP flake was mechanically exfoliated onto the

substrate by 3M scotch tape. The armchair and zigzag directions of the exfoliated BP flake was then ensured by polarized Raman spectroscopy. Then, a thin layer of PMMA is coated onto the sample (700 rpm per 5s, 4000 rpm per 60s, baking 160^{o}C for 300s). Program L-edit was used to draw the pattern on top of BP flake for etching, e-beam lithography was performed, and the sample was developed with MIBK/IPA and IPA for 30s each. The patterned Hall structure is shown in Figure 3.5a. It was carried to the ICP-RIE for etching. Detailed etching conditions will be discussed in section 3.2.2.

After etching (Figure 3.5b), the PMMA residue was washed with acetone and IPA. Next, another layer of PMMA was spin-coated with the same condition. The electron pattern of the drain-source channel in zigzag and armchair directions were produced by EBL and e-beam evaporation of 5nm/50nm of Cr/Au. The finished sample (Figure 3.5c) was finally washed with acetone and IPA to remove all unwanted PMMA residue.

Figure 3.5 (a) Hall structure before etching, **(b)** after etching, **(c)** fabricated flexible BP device.

3.3.2 Inductively Coupled Plasma – Reactive Ion Etching technique

ICP-RIE was employed to etch the BP flakes to the desired pattern shown above. It combines the chemical reactions and ion-induced etching technique, providing chemically reactive plasma to remove materials while generating high-density plasma to attract ions to the sample[73], [74].

Phantom RIE ICP from Trion Technology was used in this experiment. In this study, the effect of ICP power and RIE power were tested separately. The power range of ICP was 50W to 400W, and that of RIE was 10W to 50W. Both experimentations were set with a 10s process time. The etching results were observed with optical microscopy. The best condition tested was 250W ICP 40W RIE with a 5-20s process time. The chamber pressure was automatic and around 10mTorr. Ar and SF6 gases were used at 30sccm gas flow.

The ICP-RIE etching combines both the ICP etching and RIE etching to produce a fast, less damage, and anisotropic etching. Since the ICP-RIE etching of exfoliated BP flake has not been commonly studied, the radio frequency etching powers of both ICP and RIE is tested in this work.

The conditions of ICP etching is summarized in Figure 3.6. The optical microscopy image of 50 to 300W RF power for 10s ICP etching were compared. There is almost no

observable change after a 50W ICP etch. BP flakes etched by 100W ICP are randomly and partially etched. This can be due to the isotropic etching of merely ICP etching[73]. For RF power over 250W, BP flakes are generally etched completely. The high RF power in ICP could increase the ion bombardment on the sample surface[74]; thus, too high of the ICP power may provide surface damage on the BP. Therefore, the ICP power should be ideally set to 250W.

The RIE etching conditions were tested afterwards. The ICP etching power was controlled to 400W, RIE power of 10W to 50W were performed and contrasted. Figure 3.7 shows that most BP flakes are not etched in the cases of 10W, 20W, and 30W RIE power. On the other hand, thin BP flakes are etched with 40W and 50W RIE power. The directional electric field can attribute this near the substrate to maintain the anisotropic etching by ion plasma[73]. At the same time, the surface temperature contributed by the high ion flux has to be considered. As a result, a bare minimum of 40W RIE power was adopted to etch the sample evenly with the least surface heat-induced.

In conclusion, the BP flakes of the flexible device were etched by a 250W and 50W ICP and RIE RF power, respectively, to ensure low surface and sidewall damage with fast and low-temperature etching.

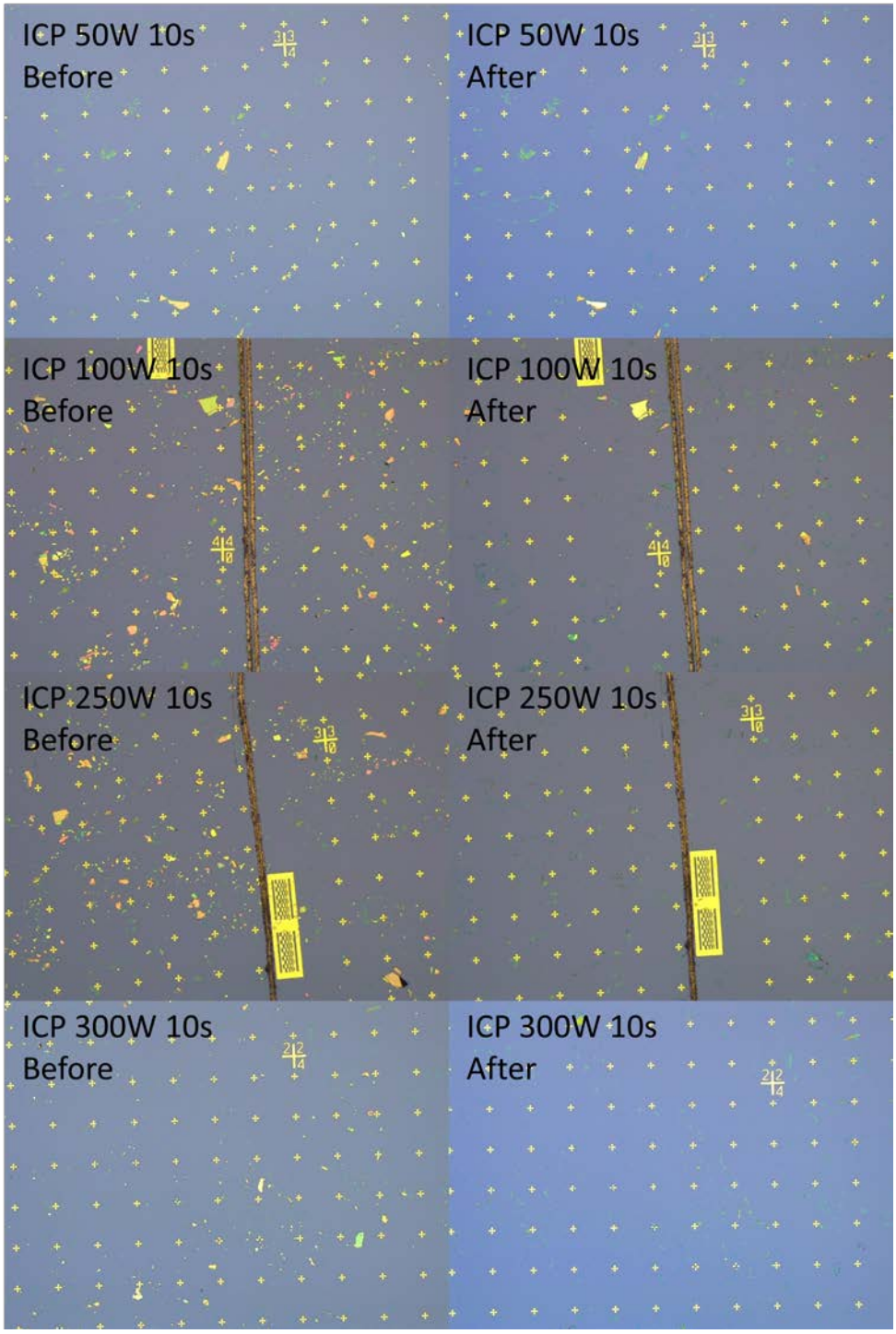

Figure 3.6 Optical Microscopy images comparison of ICP etching with 50W, 100W, 250W, and 300W RF power for 10s.

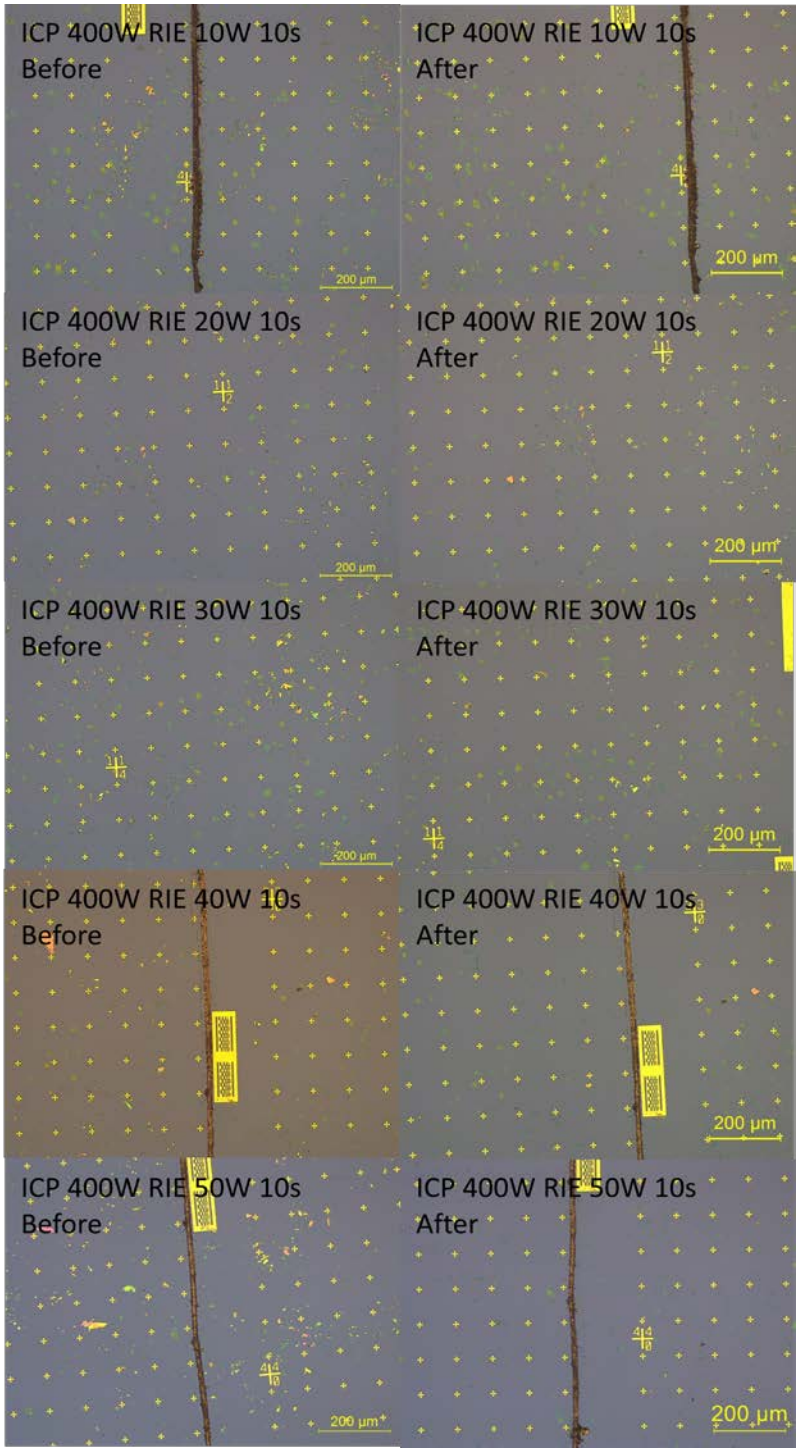

Figure 3.7 Optical Microscopy images comparison of RIE etching with 400W ICP, and 10W-50W RIE power.

3.3.3 Probe Station measurement

Keithley4200 Semiconductor Parameter Analyzer with a Lake Shore Model CRX-6.5K probe station was used to measure the current and voltage of the flexible BP device with and without bending strain. It has four 5μm vertical tips for probing and an optical microscope for fine-tuning.

3.3.4 Strain Engineering

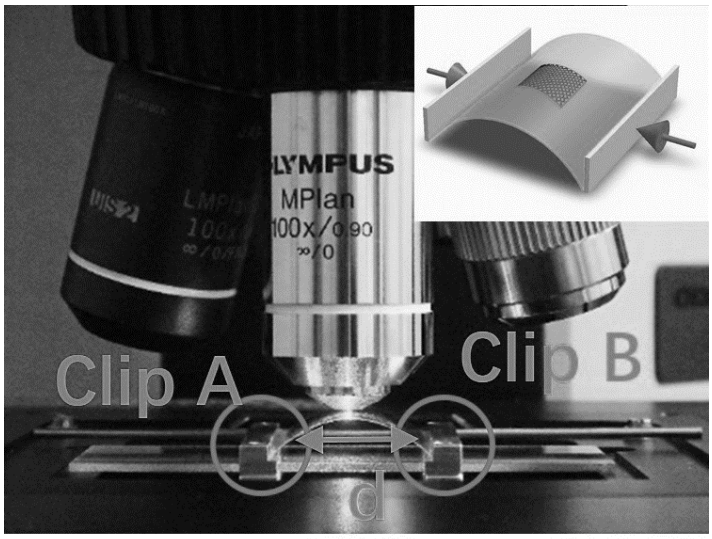

Figure 3.8 Bending strain actuator by squeezing the clips.[36]

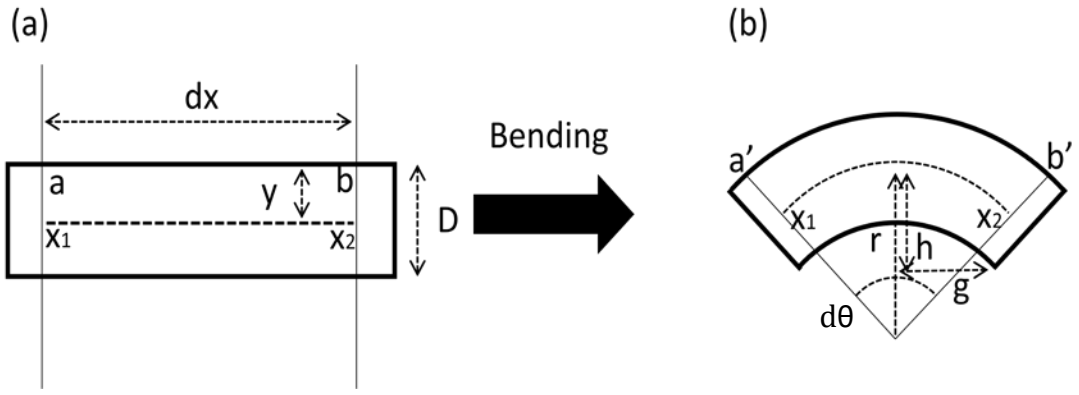

Figure 3.9 The schematic of the sample with labelled dimensions **(a)** before bending and **(b)** after bending.

The self-made bending strain actuator produced the bending strain required in this

experiment in Figure 3.8. Figure 3.9 is the schematic illustration of the sample before and after bending. Therefore, the length of the top surface before bending is

$$ab = x_1x_2 = dx = rd\theta \qquad \text{Equation 3.2}$$

and after bending, the length of the top surface becomes

$$a'b' = (r + y)d\theta \qquad \text{Equation 3.3}$$

Substitute both equations into the strain calculation

$$\varepsilon = \frac{\Delta ab}{ab} = \frac{(r + y)d\theta - rd\theta}{dx} = \frac{yd\theta}{rd\theta} = \frac{y}{r} \qquad \text{Equation 3.4}$$

Assuming the strain is merely due to bending, the bending strain can be expressed as

$$\varepsilon = \frac{D}{2r} \qquad \text{Equation 3.5}$$

The radius of curvature can be found by measuring the length of g and the vertical height from the apex shown in Figure 3.9b according to the intersecting chord theorem, where

$$g = r\sin\theta \qquad \text{Equation 3.6}$$

and

$$r - h = r\cos\theta \qquad \text{Equation 3.7}$$

By the addition of both equations

$$g^2 + (r - h)^2 = (r\sin\theta)^2 + (r\cos\theta)^2 \qquad \text{Equation 3.8}$$

$$g^2 + r^2 - 2rh + h^2 = r^2$$

$$r = \frac{g^2 - h^2}{2h}$$

The dimensions were measured without and with various bending strains. The drain-source current and drain-source voltage along the zigzag direction and armchair direction of BP were measured when the bending strain was applied along the zigzag direction and the armchair direction of the BP, respectively. The current against voltage measurement was used to find out the flexible BP device's conductance and conductivity.

Chapter 4 Characterization of Black Phosphorus

4.1 Raman Characteristics of Black Phosphorus

BP crystals were successfully synthesized by the CVT method mentioned in chapter 3. The material identification and crystallinity characterization were performed by Raman Spectroscopy and TEM, respectively. The physical dimension and appearance of the produced BP and by-product are shown in Figure 4.1a. The figure shows a shiny BP crystal with a size of around 1 centimetre. The smaller reddish-brown product is believed to be Sn_4P_3 [75]. In addition, a longer cooling time was proven to be beneficial for BP crystallization [18].

The crystal was then analyzed by Raman spectroscopy. The Raman spectrum of the bulk crystal and the mechanical exfoliated layered samples were acquired. Figure 4.1b and Figure 4.1c are the optical microscopy images of the bulk crystal and the exfoliated BP sample respectively. The Raman spectra of both samples were taken individually and summarized in Figure 4.1d. The Stokes scattering peaks of the bulk BP are 359.0 cm^{-1}, 436.8 cm^{-1}, and 463.5 cm^{-1}. These are consistent with the A_g^1, B_{2g}, and A_g^2 Raman modes

of BP mentioned in the previous studies[12], [36], [42]. The in-plane vibrations in the armchair direction, in-plane vibration of zigzag direction, and out of plane vibration are presented by the A_g^2, B_{2g}, and A_g^1 Raman responses, respectively. This confirms that the crystal synthesized by CVT is BP.

The Raman peaks of exfoliated BP are 360.3 cm^{-1}, 437.4 cm^{-1}, and 464.7 cm^{-1}. The Raman shifts of the three peaks are 1.3 cm^{-1}, 0.6 cm^{-1}, and 1.2 cm^{-1}. These shifts in Raman response could be deduced by the interaction of the interlayer van der Waals forces of BP[50].

The A_g^2 polarization of BP is shown in Figure 4.2. The BP flake in the top-left corner of Figure 4.2a was used in the experiment. The half-wave plate polarizer was turned around 360°. For each 10° polarization, the A_g^2 Raman response was taken and plotted onto Figure 4.2b. The Raman intensity should be maximum when the polarized incident laser is parallel to the atomic displacement and vice versa[51]. Since the A_g^2 mode is mainly contributed by the AC atomic displacement[36], the highest intensity Raman response indicates the ACr direction in Figure 4.2b. The orthogonal direction is then confirmed to be the ZZ orientation of BP. The increased thickness of BP flake mainly attributed to the bow-tie shape in this mode compared to the few-layer BP. Kim [51]suggested that the BP thickness can affect the Raman response due to the birefringence and dichroism of the BP

crystal in certain thickness.

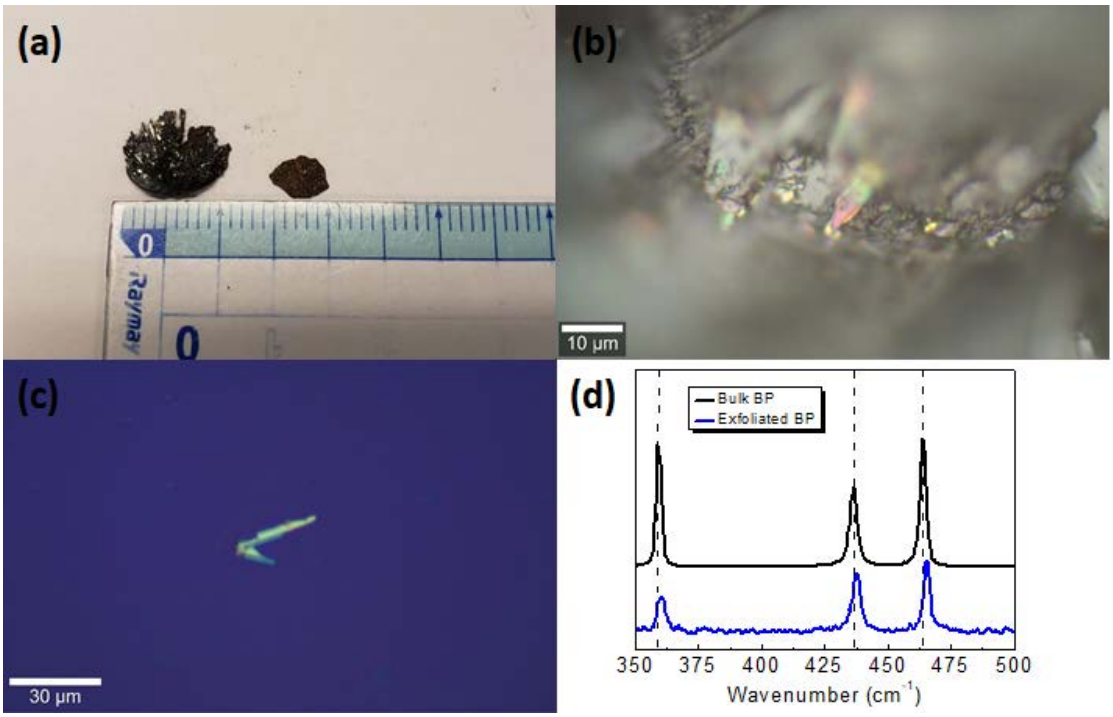

Figure 4.1 (a) Physical appearance of the CVT product, optical images of **(b)** bulk BP crystals and **(c)** an exfoliated BP flake, **(d)** Raman spectra of the bulk BP and exfoliated BP.

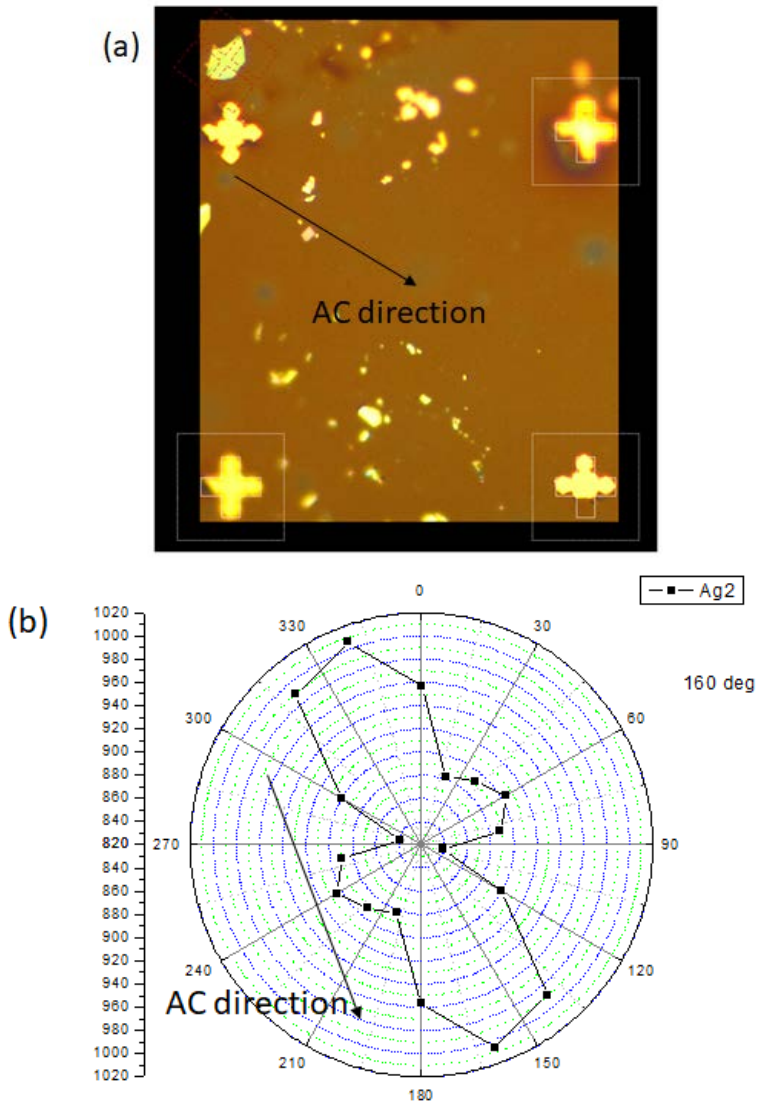

Figure 4.2 **(a)** BP flakes observed under an optical microscope, and **(b)** Raman spectroscopy Polar Plot of BP with a Polarized 532 nm laser.

4.2 Transmission Electron Microscopy Characterization

The BP crystallinity was determined by TEM characterization. Figure 4.3 is the HAADF image of the BP flake on top of a carbon-coated copper grid observed in the TEM. The thinner BP is light in colour. It is believed that the thin BP at the edges is single layer BP. The wrinkles might be caused by the transfer process of the thermal release tape. This

thermal release tape can transfer relatively large BP flakes with little damage that the EDX spectrum will further explain. SAED pattern of the BP flake is illustrated in Figure 4.4. The sharp and separable bright spots indicate the single-crystal structure of the specimen. The (010) and high intensity (110) of BP co-exist when the BP is in a single layer[76][77]. Various observable lattice planes are marked in Figure 4.4, identical to those of Wen's[76].

Figure 4.5 presents an HR-TEM image of the BP specimen. The bright lattice fringes and dark fringes correspond to the voids between atoms and phosphorus atoms. The (040) lattice plane can be seen with a 0.26nm lattice spacing according to ICDD-PDF 76-1963.

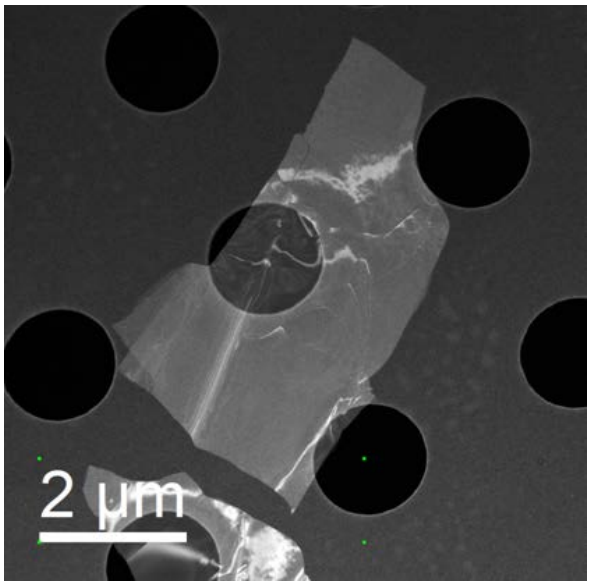

Figure 4.3 TEM image of the BP flake on a carbon-coated copper grid.

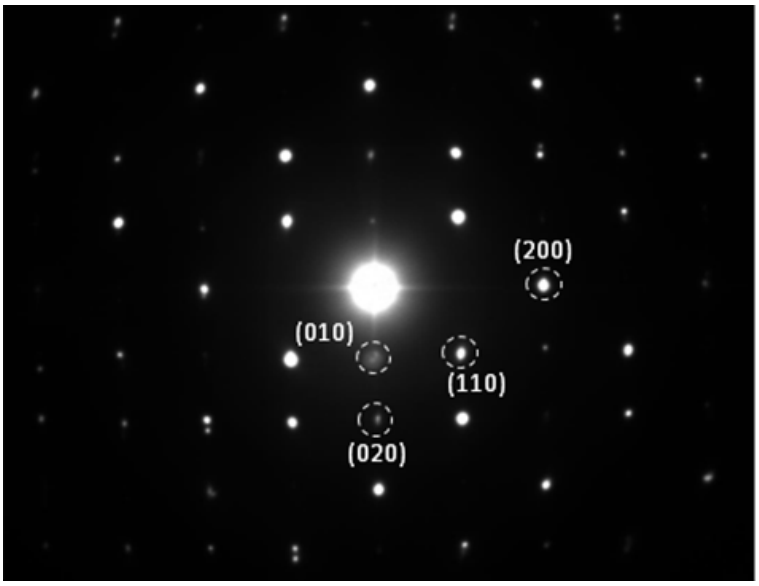

Figure 4.4 SAED pattern of the BP flake showing single crystal quality.

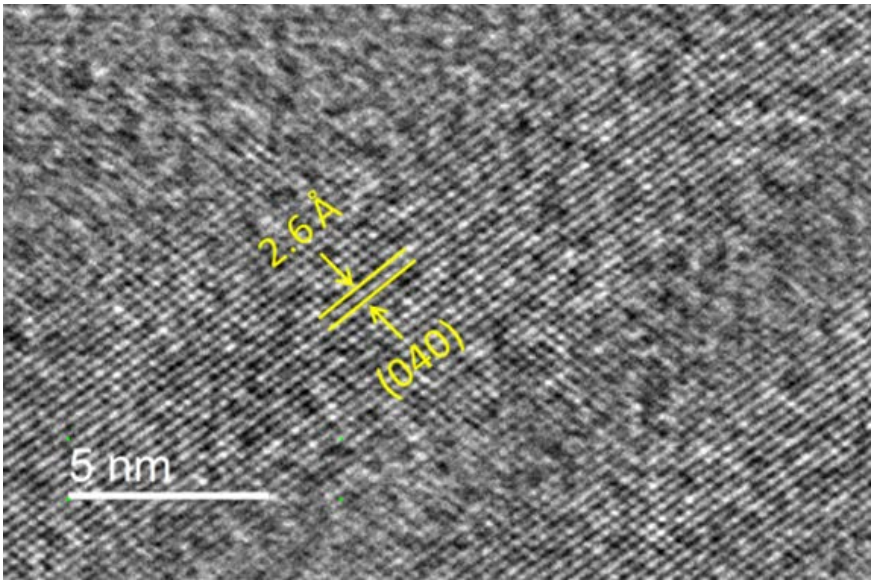

Figure 4.5 HR-TEM image of the BP flake with an observable 0.26 nm lattice spacing.

The HR-TEM image was further analyzed by using Gatan Microscopy Suite Software. A fast Fourier Transformation (FFT) was carried as shown in Figure 4.6a. All planes are filtered in Figure 4.6b. Figure 4.6c is the inverse FFT image of the (040) plane. Periodic fringes can be found in the figure. The lattice spacing is measured as illustrated in Figure 4.7. The average of multiple fringes was taken, resulting in 0.26 nm, which reconfirms

the above lattice spacing measurement.

EDX spectrum (Figure 4.8a) was taken over a selected area. Figure 4.8b indicates the measured area on the specimen. In the EDX mappings shown in Figure 4.8c and Figure 4.8d, carbon is entirely covered over the whole area while P atom is absent on the top left corner. This EDX mapping is consistent with the HAADF image of the BP flake used in this characterization. Figure 4.8a EDX spectrum is measured with no peaks omitted. Only P, Cu, and C elements are present. Therefore, it confirms that there is little oxidation during the transfer process. It can be compared to the previously used direct transfer method[78], and PDMS stamping[79], the direct transfer of BP on the TEM grid was proven to be difficult due to adhesion of BP and carbon, and PDMS stamping inevitably introduces oxygen on the specimen via siloxanes presented in the PDMS, while both of these problems are not found in the method used in this study.

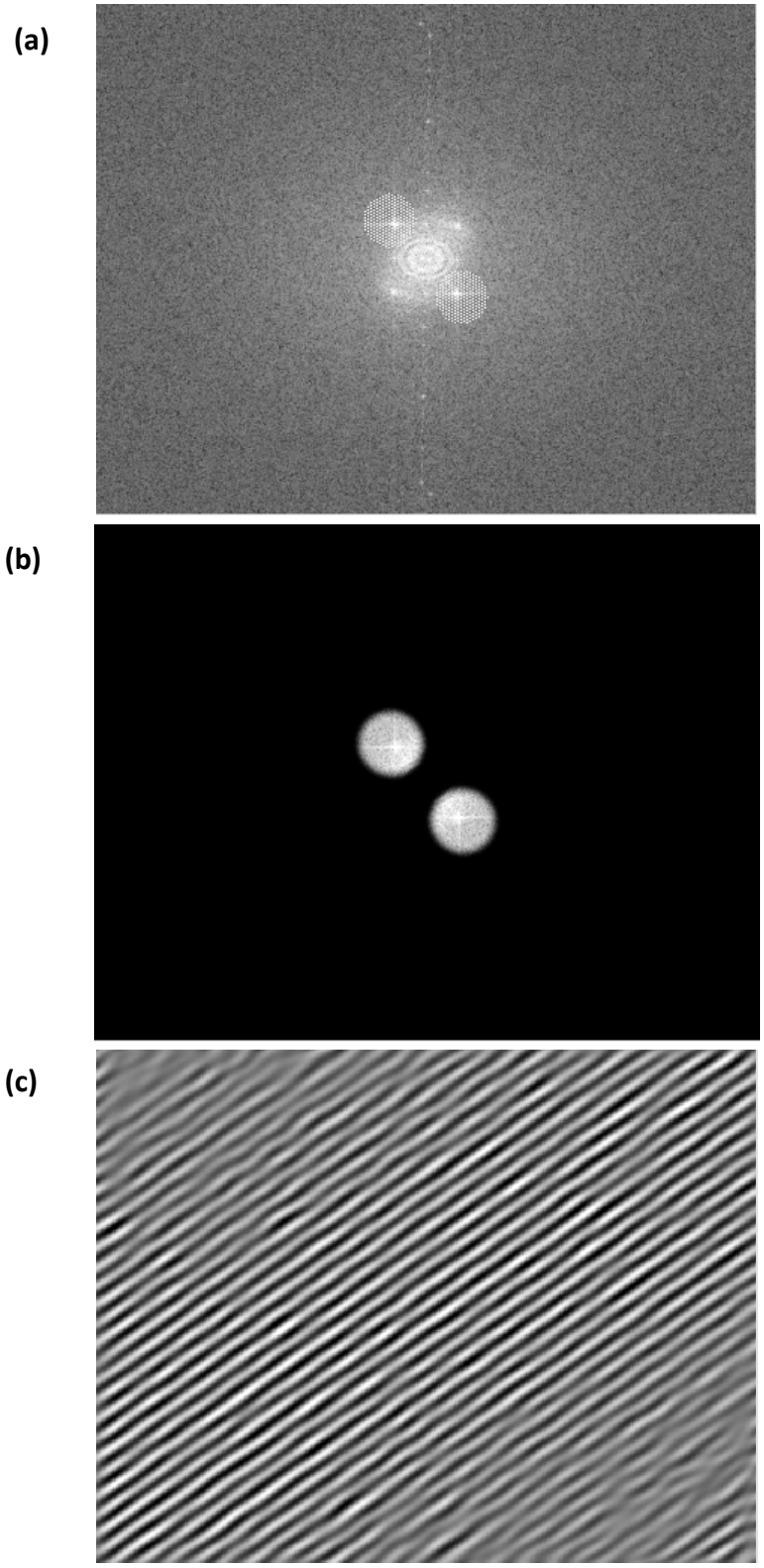

Figure 4.6 (a) FFT Image, **(b)** masked FFT image, **(c)** inverse FFT image of the BP.

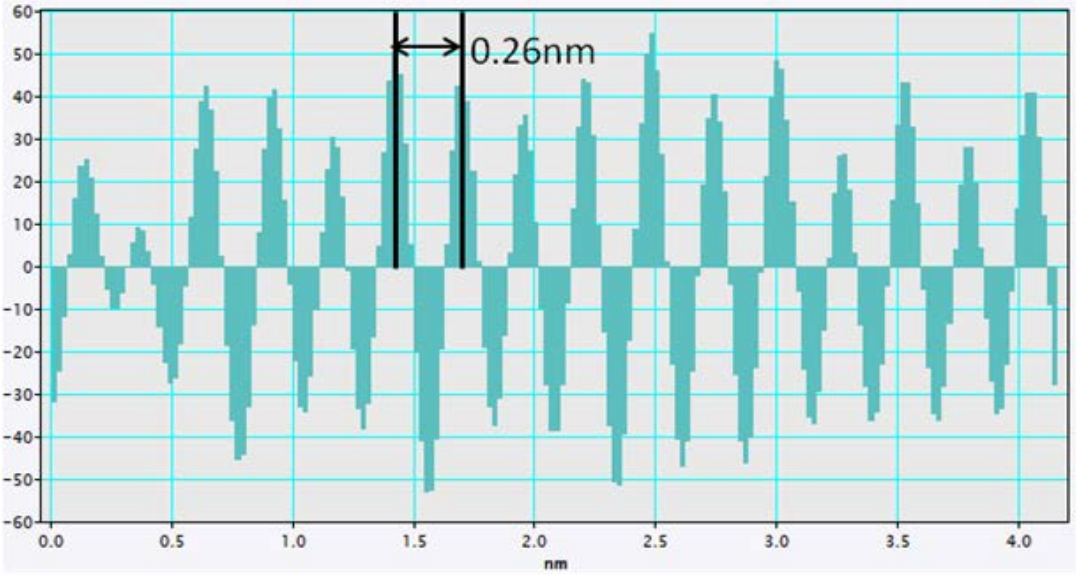

Figure 4.7 Profile plot of the inverse FFT with lattice spacing measurement.

(a)

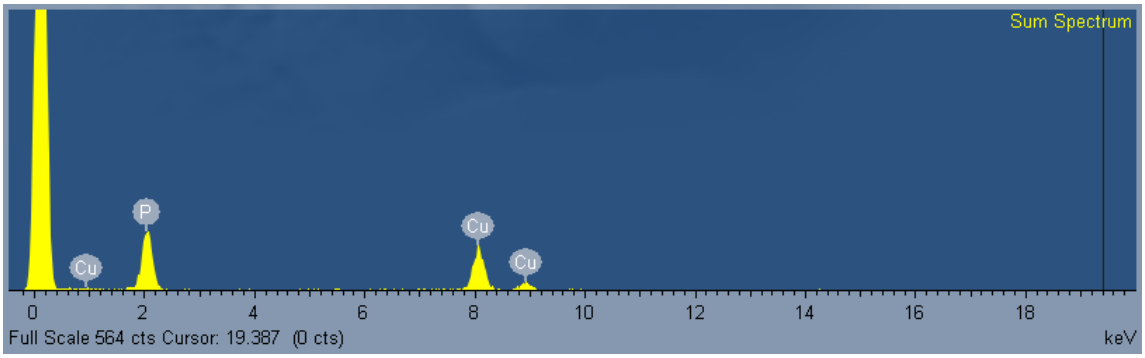

(b)

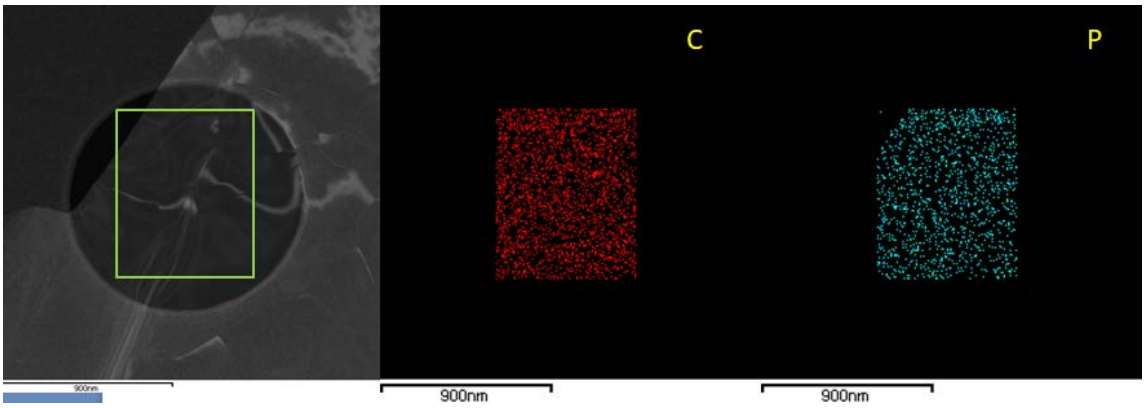

Figure 4.8 **(a)** EDX spectrum of the BP crystal, **(b)** selected area of EDX mapping.

Chapter 5 Black Phosphorus Synthesis by Molecular Beam Epitaxy

5.1 Growth Observations

During the MBE BP synthesis process, it was found that BP crystal releases atoms at 260 ^{o}C or above and that of GaP is above 780 ^{o}C (conditions listed in Table 6.1). The reported decomposition temperature of GaN and GaAs are 900 ^{o}C[80] and 480 ^{o}C[81], respectively. The observed decomposition temperature of GaP in this work is in between GaN and GaAs. Gallium and phosphorous have different vapour pressure. At 780 ^{o}C, it decomposes, and the covalent bond is broken. Vaporized phosphorous is diffused to the substrate while Gallium remains in the liquid state. The substrate temperature was varied to observe the distinct uniformity of the grown BP.

In the attempt to use BP as the source material, no observable P cluster was shown on the substrate. Figure 5.1 is the picture of the effusion cell of the BP source after the growth. Yellow stains are observed on the covering ring and the top of the metal heating shield. The phase conversion of BP may explain it. BP may be changed to other phosphorus allotropes when heated in a low-pressure environment[38].

The source material was changed to GaP. Figure 5.2 is the physical image of the mica substrate before and after the MBE growth. Yellowish-brown colour on the whole substrate surface except the edge that sample holder covered can be seen on the mica after the growth. As a result, the MBE BP produced from GaP is transferred to Raman spectroscopy, AFM, and XRD for characterization.

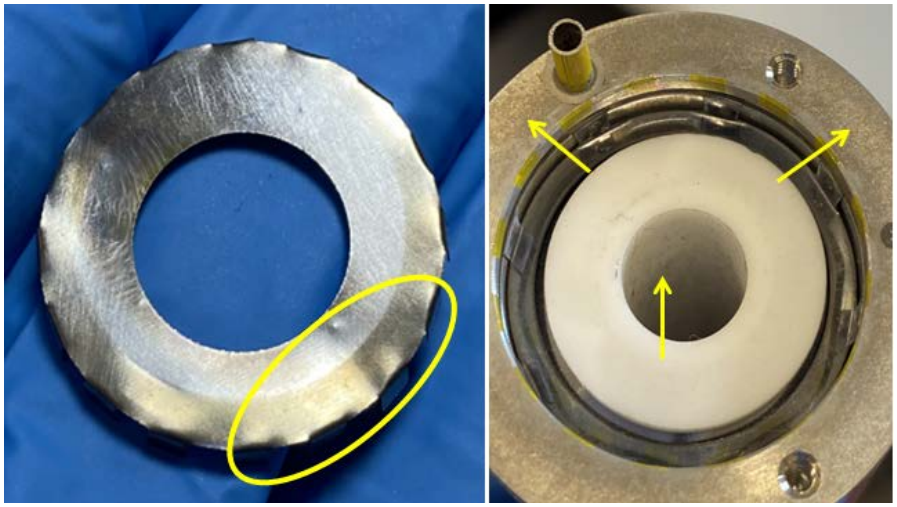

Figure 5.1 Photos showing yellow stains and black dots on the Effusion cell covering ring, crucible, and metal heating shield.

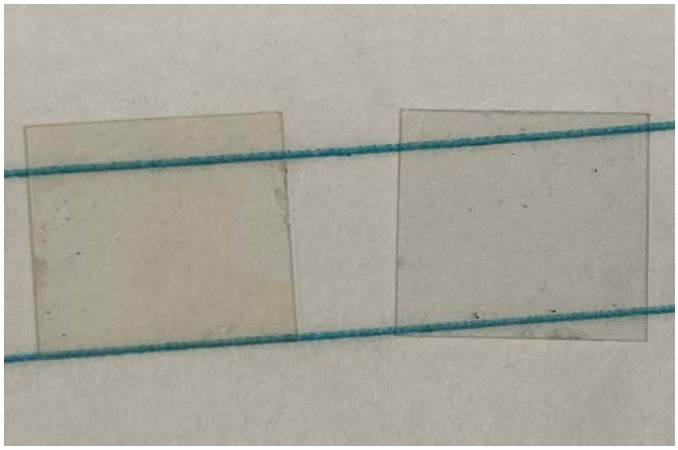

Figure 5.2 Physical Observation of mica substrate before (right) and after (left) MBE growth.

5.2 Characterization

The MBE grown BP samples on SiO_2 by GaP with room temperature and 160 ^oC substrate were testified by Raman Spectroscopy (Figure 5.3) and AFM (Figure 5.4). Figure 5.3a shows the Raman spectrum of BP grown with no substrate heat. The Raman peaks of BP can be barely observed. The response is not prominent when compared to the background noise. The Raman response of BP grown with a 160 ^oC substrate temperature is fairly more distinguishable in Figure 5.3b. The FWHM of the peaks is narrower compared to that of Figure 5.3a. This suggests that the MBE BP grown in this condition has a certain degree of crystallinity rather than amorphous in form. The spectrum can be compared with the results obtained in PLD BP. The amorphous PLD BP produced by Yang[27] has a broader FWHM similar to Figure 5.3a, whereas the polycrystalline BP produced by Wu[28] has a result similar to Figure 5.3b.

The AFM images in Figure 5.4 demonstrate the surface morphology of the MBE BP. As shown in Figure 5.4a-c, the BP is formed as clusters with few-tens of nanometer in lateral dimension when the substrate temperature is at room temperature. The size and the distribution of the BP clusters are random. The few nanometer thick clusters advocate that the temperature gradient of the MBE diffusion might be too high in this situation. In the sample grown at 160^o C substrate temperature, the AFM images (Figure 5.4d-e) show

a smoother surface with reduced thin thickness than the previous sample. However, the uniformity of the film thickness is still limited.

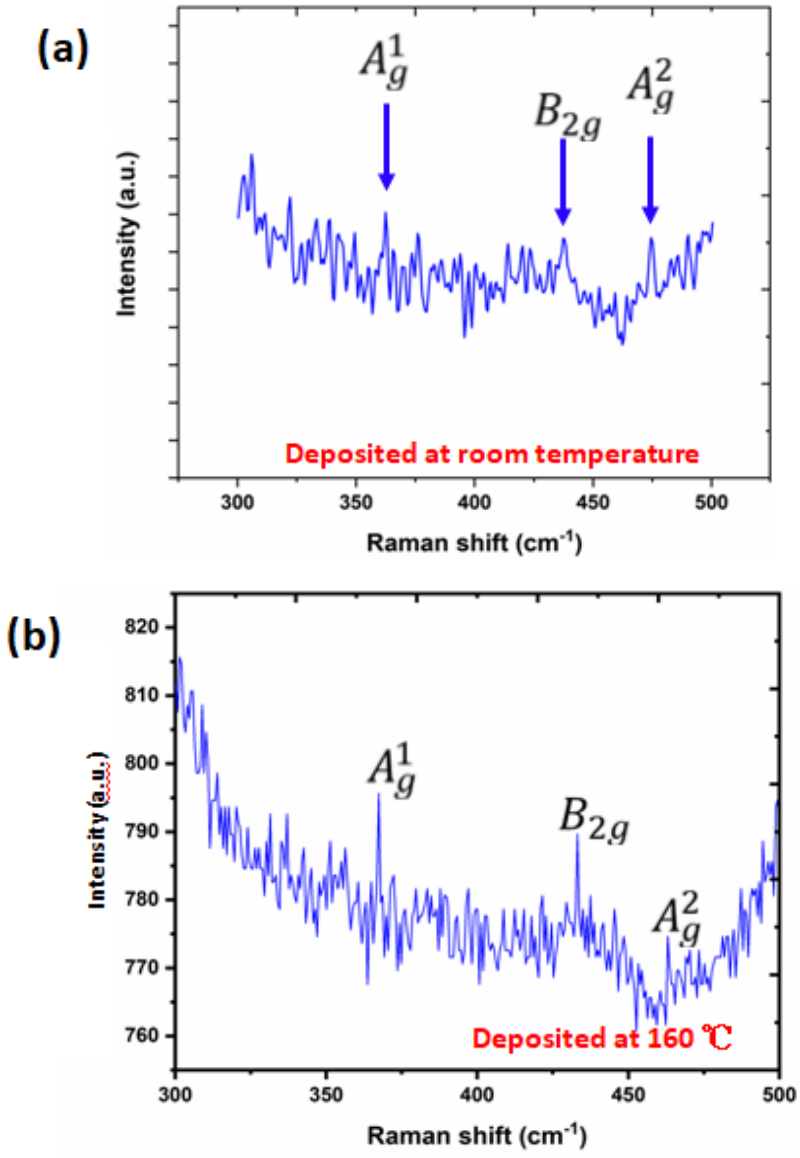

Figure 5.3 Raman spectrum of the MBE grown BP on SiO_2 with a substrate temperature of **(a)** room temperature, and **(b)** 160 °C.

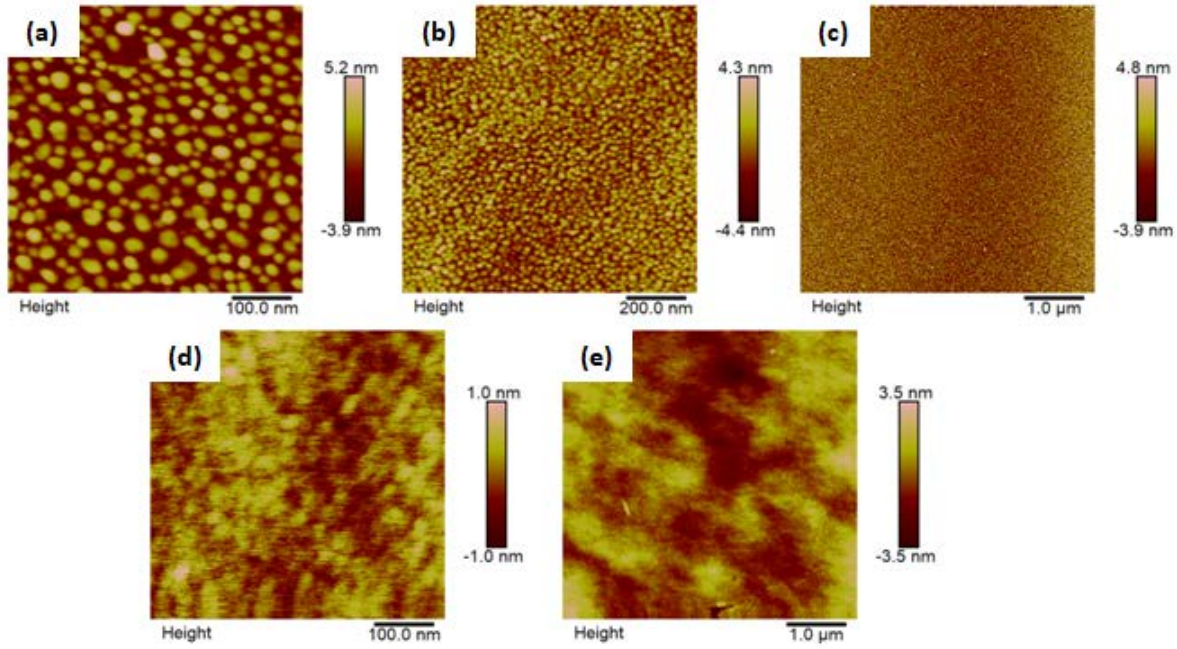

Figure 5.4 AFM images of MBE grown BP on SiO_2 with a substrate temperature of **(a-c)** room temperature, and **(d-e)** 160 ^oC.

An XRD characterization of the thin film BP on SiO_2 with a 160 ^oC substrate temperature was conducted to verify the BP structure and elemental content. Figure 5.5a is an XRD spectrum of the sample tested immediately after being removed from the load-lock in the MBE. Peaks of black phosphorus structure are observed with reference to JCPDS card no. 01-073-1358. Only BP is observed on the surface, which reaffirms that gallium is not diffused. The XRD spectrum of the same sample was measured after two weeks of storage in a vacuum container shown in Figure 5.5b. Although it is stored in a vacuum environment, the sample BP still decomposed after 2 weeks. This result suggests that the film thin grown by MBE is not stable in ambient condition. Previous research claims that

the contact of both air, which contain water molecules, and light would result in oxidation with BP to form phosphorus oxide (P_xO_y) [63]. The decomposed BP thin film will have P atoms removed from the flake, which also reduce channel contact or increase the channel resistance of the sample. Hence, the BP thin film by MBE would have its electrical conductivity reduces drastically within hours of contact with air. As a result, the uniformity and stability of the grown BP thin film are still lacking.

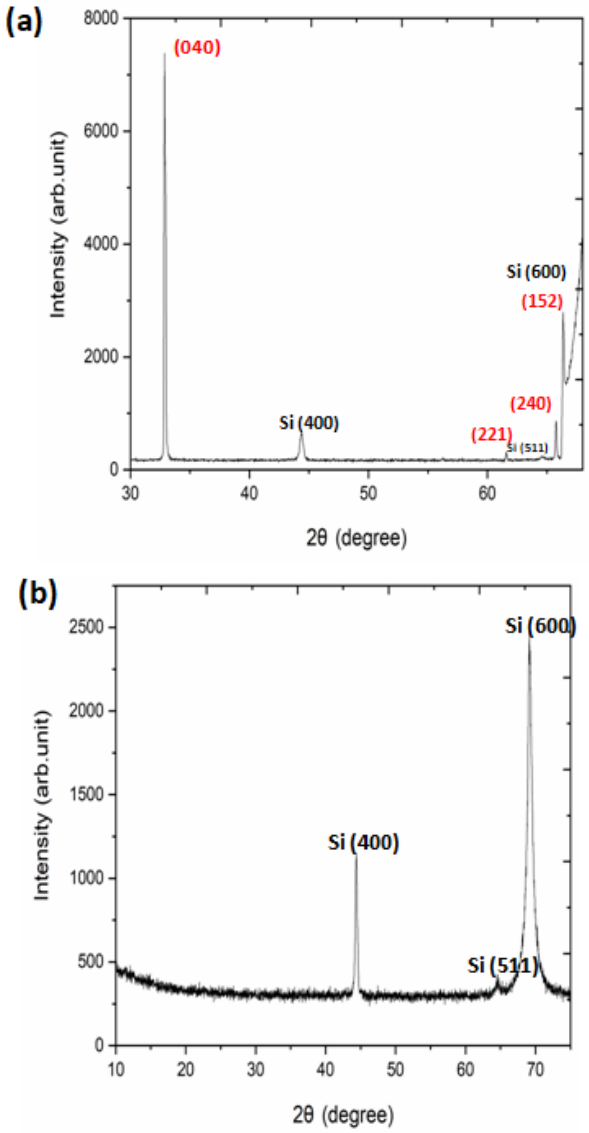

Figure 5.5 XRD spectrum of the BP grown on SiO_2 with 160 ºC substrate temperature **(a)** as-prepared, and **(b)** after two weeks.

Another attempt was to use mica substrate with a 300 ºC substrate temperature. The substrate temperature and substrate were used as stated in the PLD BP[28]. The cleaved surface of mica has a closely packed hexagonal atomic pattern and is atomically smooth[82], and the substrate temperature at 300 ºC was attempted to produce a more uniform BP thin film. The XRD spectrum of BP and mica in Figure 5.6 is homogeneous with the XRD result obtained by Wu[28]. The observed BP peaks imply the large-scale high crystallinity of the orthorhombic structure of BP, with space group cmca.

The results suggest that GaP is suitable source material, and mica is a better substrate for the epitaxial growth of BP by MBE. In addition, the temperature gradient of the MBE diffusion should be carefully controlled to synthesize a large area of uniform BP thin film with good crystal quality.

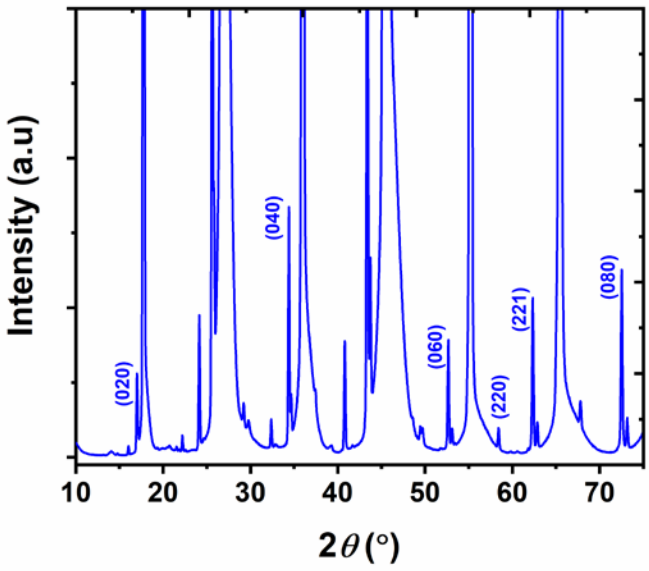

Figure 5.6 XRD spectrum of the BP grown on mica with 300 ºC substrate temperature.

Chapter 6 Strain Effect on Flexible Black Phosphorus Device

The conductance measurement of BP under the uniaxial strain was performed on the flexible BP device patterned on the PI substrate, as shown in Figure 6.1a The ZZ and AC orientations of the exfoliated BP sample were first characterized by Raman spectroscopy. The polar plot in Figure 6.1b shows that the A_g^2 Raman mode of the BP flake is at a maximum of 140^o (y-axis). It represents the large AC atomic displacement in A_g^2 mode [36], and thus, the perpendicular x-axis is the ZZ direction. Both orientations were recorded and subsequently, Hall patterned, illustrated by the red-dotted line on Figure 6.1a produced by EBL. The finished BP device can be seen in Figure 6.1c, where two electrodes were connected to the AC direction and ZZ direction, respectively.

The device performance was then tested by the probe station measurement. The actuator provided a tensile bending strain between 0% to about 1.4% on the AC and ZZ directions of the BP. The drain-source current and voltage of both AC and ZZ directions were measured for each point of strain given. Figure 6.2 shows the IV measurement along with AC and ZZ directions without strain. The current response of both directions was

measured with -50 mV to 50 mV voltage bias. The IV is linear in both AC and ZZ directions, and the corresponding linear fit equations can calculate conductance in ZZ and AC. The calculated conductance without strain in AC and ZZ directions are 4.43μS, 1.01μS, respectively. The conductance in the AC direction is around 4.4 times that of the ZZ direction. The difference in conductance can be explained by the anisotropy of BP, where the AC orientation is the preferred electrical path in BP [37]. The effective mass of BP along the AC direction is 6-8 times smaller than that of the ZZ direction[83], so it also suggests that the mobility and conductivity of BP along the AC direction are expected to be higher. Therefore, it attributed to the conductance ratio of BP without strain is 4.4 in this experiment.

The IV measurements in both directions were then carried on with different strain applied along AC and ZZ directions. The conductance with different applied strain along AC and ZZ directions is summarised in Figures 6.3a and 6.3b. The electrical conductance along both orientations reduces when strain was applied in either direction because the strain applied stretched and deformed the structure of BP, the path of electron with be modified to another direction that contribute to the decrease of electrical conductance [37].It shows that the effect of strain is more obvious in the change of conductance in the AC direction.

In Figure 6.3a, the conductance in the AC direction rapidly drops to around one-sixth of the original value and is reduced by one order of magnitude with 1.4% strain applied in the AC direction. Whereas the conductance in the ZZ direction has a more gentle decrease, it has a quarter of its original conductance with 1.4% strain in the AC direction. A similar result can be seen in Figure 6.3b, where the strain is applied in the ZZ direction instead. The conductance in the AC and ZZ directions at 1.4% strain is reduced to 0.15 μS and 0.5 μS. It is suggested that the asymmetric modulation in BP provides a stronger piezoelectric effect in the AC orientation[33], oppositely, a more substantial piezo-resistive effect in ZZ orientation. The BP FET fabricated by Ma[33] also has a similar result in the drain current and drain voltage measurement. The IV response in the AC direction is larger than that of the ZZ direction with applied strain. However, the results obtained did not have a switch in spatial preference of electrical conductance. It may be due to the limited strain used in the experiment. The uniaxial strain did not reach the critical value of 5-6 % stated in the theoretical study [37]. The transition electrical conductance in the ZZ orientation was unfortunately missing.

To further analyze the obtained result, the strain in the AC and ZZ directions with AC and ZZ bias measurements are rearranged into Figure 6.4a and Figure 6.4b. Figure 6.4a

shows that the direction of strain applied has minimal impact on the conductance in the AC direction. The change in conductance along AC direction with AC strain and ZZ strain are almost identical, while the direction of provided strain has a more distinct influence on the conductance in ZZ direction illustrated in Figure 6.4b. The conductance measured along the ZZ direction with a given ZZ strain has a smaller decrease than other circumstances. The conductance along the ZZ direction is only halved with 1.4% strain while about 20% of the conductance remain after applying the strain in other cases, as shown in Figure 6.4a and 6.4b. It could result from the change in the lowest energy state of the conduction band in BP, which is unique in the ZZ direction with a given strain along ZZ, according to the DFT/PBE simulation in Fei's and Yang's works[37]. This can be a trace of the transition of electrical conductance if the given strain is large enough in this experiment.

To sum up, the conductance varied by uniaxial strain was realized. It is proven that the conductance of BP in the AC direction is larger than that of the ZZ direction. In addition, the electrical response in AC orientation is stronger with an applied strain. Most importantly, the conductance with ZZ uniaxial strain along ZZ direction differs from the other cases may be attributed to the possibility of anisotropic electrical conductance

transition, which further study is required.

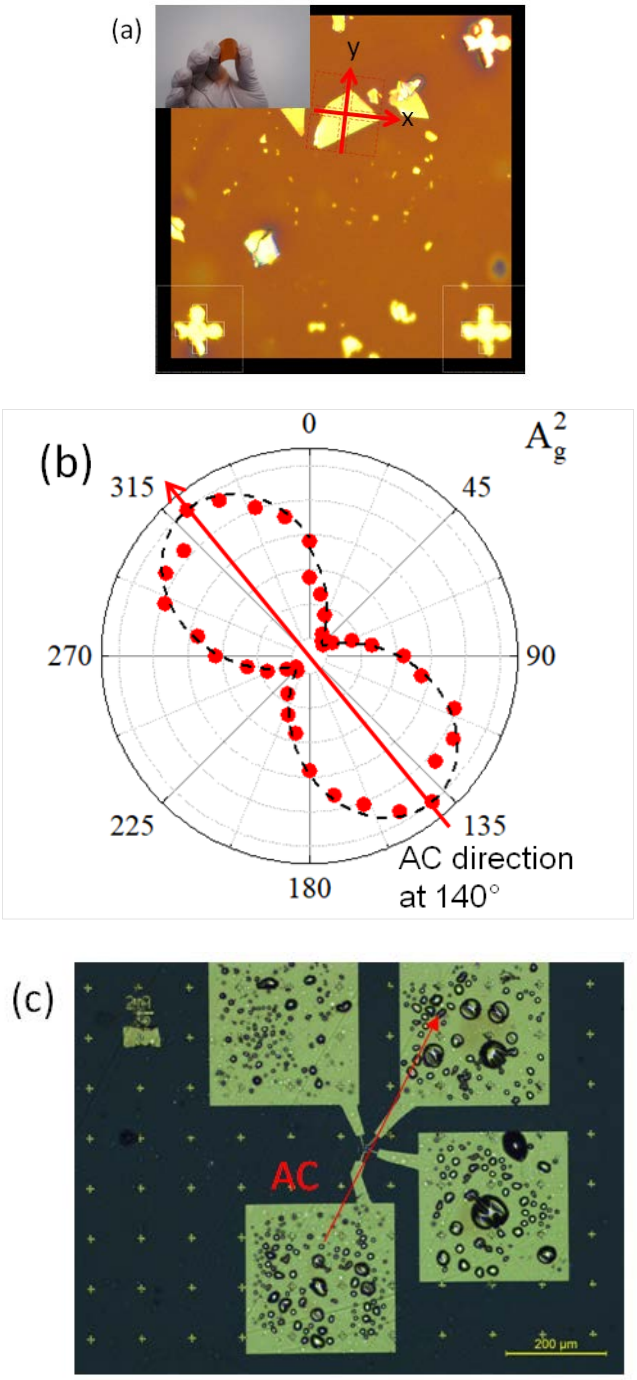

Figure 6.1 (a) Optical image of the BP flake with ZZ and AC orientation (x-y axis) and the Hall pattern (red-dotted line); **(b)** Polar plot of the BP flake; **(c)** optical image of the fabricated device.

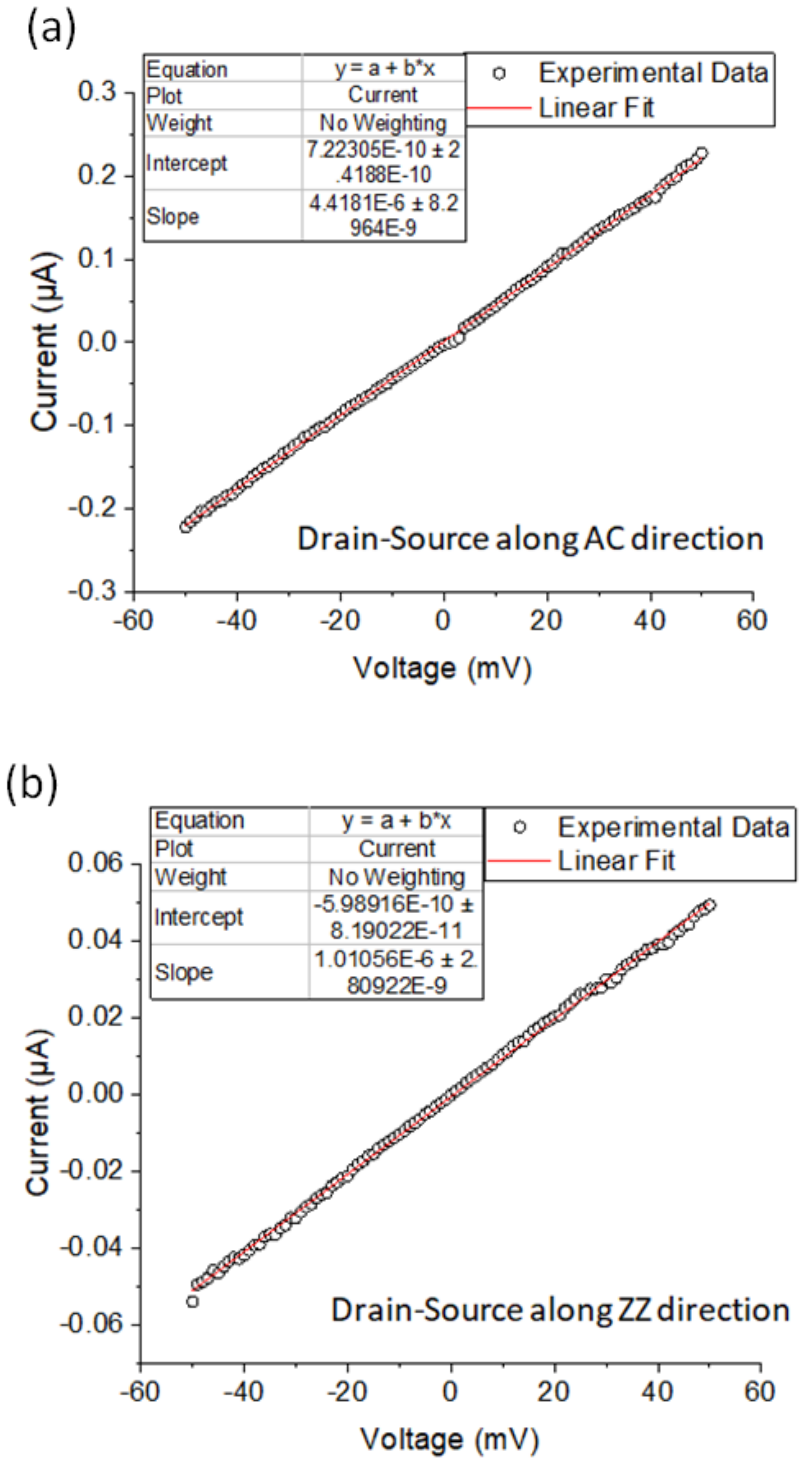

Figure 6.2 IV graph with linear fit with drain-source along the **(a)** AC, and **(b)** ZZ directions.

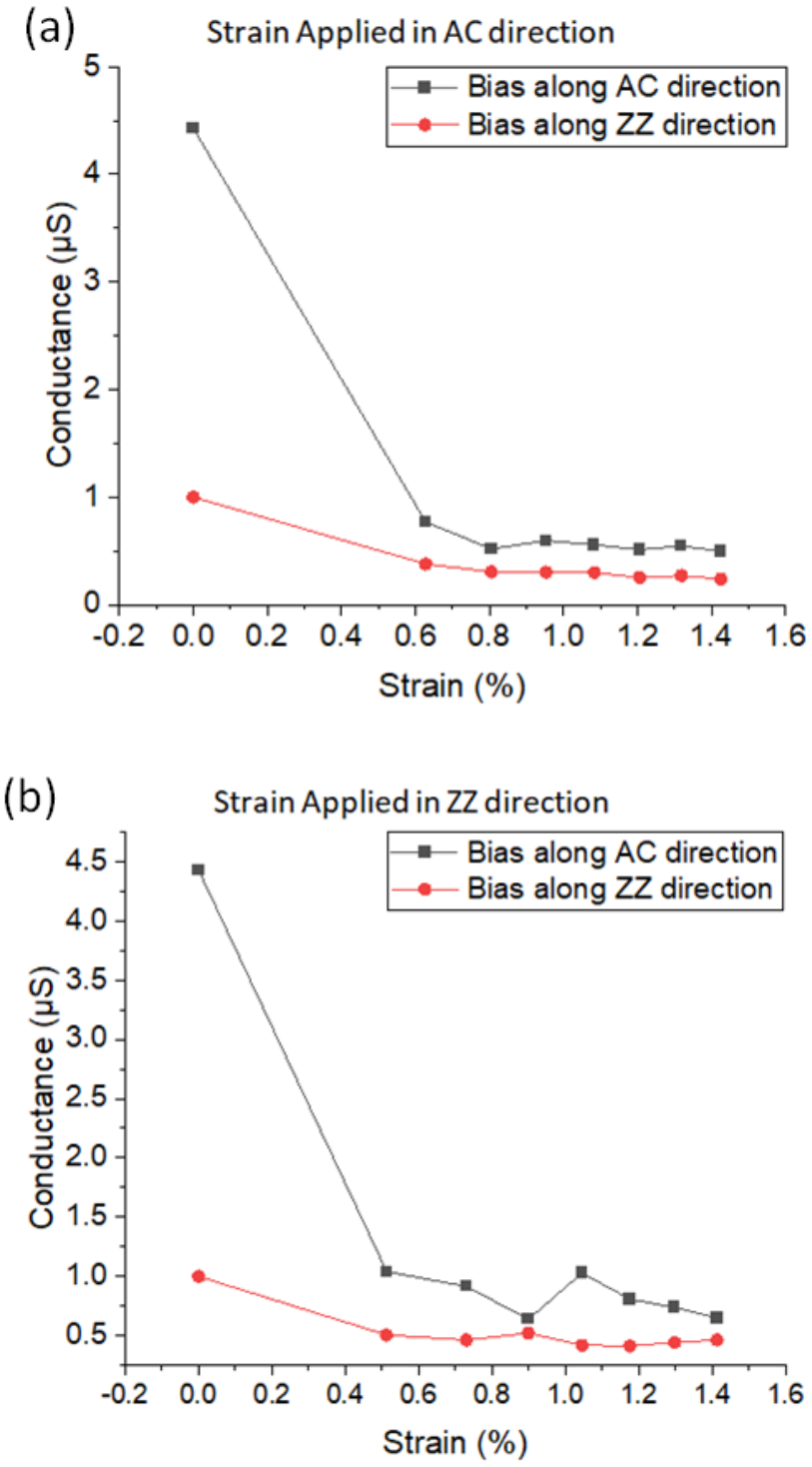

Figure 6.3 Conductance induced by the uniaxial strain along the AC and ZZ directions with strain applied in the **(a)** AC , and **(b)** ZZ directions.

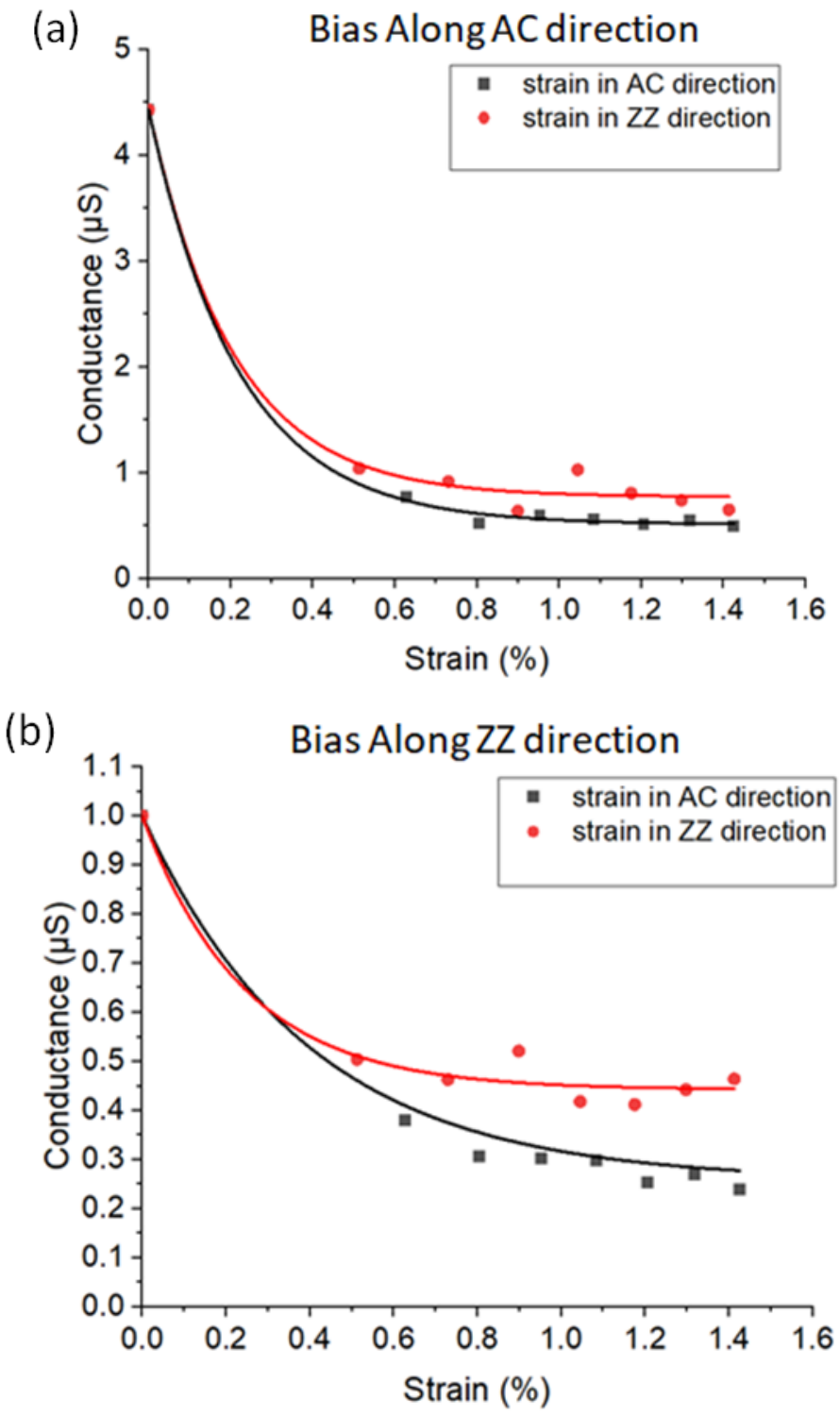

Figure 6.4 Conductance induced by AC direction and ZZ direction uniaxial strain along the **(a)** AC, and **(b)** ZZ directions.

Chapter 7 Conclusion and Future Works

7.1 Conclusion

To summarize this research study, three main objectives have been achieved. Firstly, the synthesis of BP crystal from the CVT method was conducted. A vacuum-sealed tube with a combination of RP, Sn, and I_2 precursors was used to produce high crystal quality and centimetre-scale BP crystal by heating it to 600 ^{o}C and slowly cooling down to room temperature for good crystallization. Secondly, 2D MBE BP in centimetre scale on mica substrate is partially achieved. Although thin-film BP quality can still be improved, large area thickness uniformity and crystallinity of the synthesized BP thin film were testified by XRD, AFM and Raman. Thirdly, the conductance of BP under uniaxial strain was analyzed by the fabricated flexible BP device on PI substrate. Electrical conductance drops exponentially with uniaxial strain applied. Noticeably, the conductance along the ZZ direction when using the ZZ strain is different to that of other circumstances. It agrees with the theory that the spatial preference of electrical conductance in BP only occurs when applying strain in the ZZ direction.

These results are significant to the future development of BP in the research field, and hopefully, in industrial and commercial applications. The realization of large-area BP thin

film by the MBE could provide a more intuitive and faster way to grow uniform 2D BP with good crystal quality and hence hopefully increase the popularity and viability of BP in optoelectronics and microelectronics development. For example, large area 2D BP can be used to manufacture infrared photodetector, fast speed field-effect transistor, and flexible or wearable BP. Furthermore, a flexible BP device could be applied to electro-mechanical applications. Different responsiveness of the piezoelectric BP device can be achieved by a directional modulation between ZZ and AC orientations.

7.2 Future works

Further research on MBE BP device fabrication is suggested to fully understand its optoelectrical properties and explore the possible applications of this 2D BP. Furthermore, the strain effect on flexible BP studied in this work is limited by a few processes, such as the inevitable damage of the BP from ICP-RIE etching may hinder the electrical performance of BP, and the partial strain induced by the vacuum chamber during measurement as the compensation of less air degradation. Therefore, future works on etching damage analysis and strain measurement in the noble gas chamber are recommended.

References

[1] K.Novoselov *et al.*, "Electric Field Effect in Atomically Thin Carbon Films," *Science (American Association for the Advancement of Science)*, vol. 306, no. 5696, pp. 666-669, 2004.

[2] R.Ma and T.Sasaki, "Two-dimensional oxide and hydroxide nanosheets: Controllable high-quality exfoliation, molecular assembly, and exploration of functionality," *Acc. Chem. Res.*, vol. 48, no. 1, pp. 136–143, 2015.

[3] K. F.Mak, C.Lee, J.Hone, J.Shan, and T. F.Heinz, "Atomically thin MoS_2: A new direct-gap semiconductor," *Phys. Rev. Lett.*, vol. 105, no. 13, pp. 2–5, 2010.

[4] J.Feng, X.Qian, C. W.Huang, and J.Li, "Strain-engineered artificial atom as a broad-spectrum solar energy funnel," *Nat. Photonics*, vol. 6, no. 12, pp. 866–872, 2012.

[5] H. S.Lee *et al.*, "MoS_2 nanosheet phototransistors with thickness-modulated optical energy gap," *Nano Lett.*, vol. 12, no. 7, pp. 3695–3700, 2012.

[6] Y.Ye *et al.*, "Exciton-dominant electroluminescence from a diode of monolayer MoS_2," *Appl. Phys. Lett.*, vol. 104, no. 19, 2014.

[7] X.Miao *et al.*, "High efficiency graphene solar cells by chemical doping," *Nano*

Lett., vol. 12, no. 6, pp. 2745–2750, 2012.

[8] G.Wang, X.Shen, J.Yao, and J.Park, "Graphene nanosheets for enhanced lithium storage in lithium ion batteries," *Carbon N. Y.*, vol. 47, no. 8, pp. 2049–2053, 2009.

[9] J. J.Yoo *et al.*, "Ultrathin planar graphene supercapacitors," *Nano Lett.*, vol. 11, no. 4, pp. 1423–1427, 2011.

[10] H.Liu *et al.*, "Phosphorene: An unexplored 2D semiconductor with a high hole mobility," *ACS Nano*, vol. 8, no. 4, pp. 4033–4041, 2014.

[11] P. W.Bridgman, "Two new modifications of phosphorus," *J. Am. Chem. Soc.*, vol. 36, no. 7, pp. 1344–1363, 1914.

[12] H. B.Ribeiro, M. A.Pimenta, and C. J. S.de Matos, "Raman spectroscopy in black phosphorus," *J. Raman Spectrosc.*, vol. 49, no. 1, pp. 76–90, 2018.

[13] S.Das, W.Zhang, M.Demarteau, A.Hoffmann, M.Dubey, and A.Roelofs, "Tunable transport gap in phosphorene," *Nano Lett.*, vol. 14, no. 10, pp. 5733–5739, 2014.

[14] P. W.Bridgman, "Rough Compressions of 177 Substances to 40,000 Kg/Cm^2," *Proc. Am. Acad. Arts Sci.*, vol. 76, no. 3, pp. 71–87, 1948.

[15] T.Bao, O.Tegus, Hasichaolu, J.Ning, and Narengerile, "Preparation of black phosphorus by the mechanical ball milling method and its characterization," *Solid*

State Phenom., vol. 271 SSP, pp. 18–22, 2018.

[16] M.Baba, F.Izumida, Y.Takeda, and A.Morita, “Preparation of Black Phosphorus Single Crystals by a Completely Closed Bismuth-Flux Method and Their Crystal Morphology,” *Jpn. J. Appl. Phys.*, vol. 28, no. Part 1, No. 6, pp. 1019–1022, 1989.

[17] S.Lange, P.Schmidt, and T.Nilges, “Au_3SnP_7@Black Phosphorus: An easy access to black phosphorus,” *Inorg. Chem.*, vol. 46, no. 10, pp. 4028–4035, 2007.

[18] M.Zhao *et al.*, “Growth Mechanism and Enhanced Yield of Black Phosphorus Microribbons,” *Cryst. Growth Des.*, vol. 16, no. 2, pp. 1096–1103, 2016.

[19] A.Ciesielski and P.Samorì, “Graphene via sonication assisted liquid-phase exfoliation,” *Chem. Soc. Rev.*, vol. 43, no. 1, pp. 381–398, 2014.

[20] G.Qu *et al.*, “Improved Biocompatibility of Black Phosphorus Nanosheets by Chemical Modification,” *Angew. Chemie - Int. Ed.*, vol. 56, no. 46, pp. 14488–14493, 2017.

[21] D.Hanlon *et al.*, “Liquid exfoliation of solvent-stabilized few-layer black phosphorus for applications beyond electronics,” *Nat. Commun.*, vol. 6, 2015.

[22] P.Yasaei *et al.*, “High-Quality Black Phosphorus Atomic Layers by Liquid-Phase Exfoliation,” *Adv. Mater.*, vol. 27, no. 11, pp. 1887–1892, 2015.

[23] C.Hao *et al.*, “Flexible All-Solid-State Supercapacitors based on Liquid-Exfoliated

Black-Phosphorus Nanoflakes," *Adv. Mater.*, vol. 28, no. 16, pp. 3194–3201, 2016.

[24] A.Ambrosi, Z.Sofer, and M.Pumera, "Electrochemical Exfoliation of Layered Black Phosphorus into Phosphorene," *Angew. Chemie - Int. Ed.*, vol. 56, no. 35, pp. 10443–10445, 2017.

[25] W.Lin, Y.Lian, G.Zeng, Y.Chen, Z.Wen, and H.Yang, "A fast synthetic strategy for high-quality atomically thin antimonene with ultrahigh sonication power," *Nano Res.*, vol. 11, no. 11, pp. 5968–5977, 2018.

[26] J. B.Smith, D.Hagaman, and H. F.Ji, "Growth of 2D black phosphorus film from chemical vapor deposition," *Nanotechnology*, vol. 27, no. 21, 2016.

[27] Z.Yang *et al.*, "Field-Effect Transistors Based on Amorphous Black Phosphorus Ultrathin Films by Pulsed Laser Deposition," *Adv. Mater.*, vol. 27, no. 25, pp. 3748–3754, 2015.

[28] Z.Wu *et al.*, "Large-scale growth of few-layer two-dimensional black phosphorus," *Nat. Mater.*, 2021.

[29] J. L.Zhang *et al.*, "Epitaxial Growth of Single Layer Blue Phosphorus: A New Phase of Two-Dimensional Phosphorus," *Nano Lett.*, vol. 16, no. 8, pp. 4903–4908, 2016.

[30] C.Gu *et al.*, "Growth of Quasi-Free-Standing Single-Layer Blue Phosphorus on Tellurium Monolayer Functionalized Au(111)," *ACS Nano*, vol. 11, no. 5, pp. 4943–4949, 2017.

[31] W.Zhang *et al.*, "Epitaxial Synthesis of Blue Phosphorene," *Small*, vol. 14, no. 51, pp. 1–6, 2018.

[32] J. P.Xu, J. Q.Zhang, H.Tian, H.Xu, W.Ho, and M.Xie, "One-dimensional phosphorus chain and two-dimensional blue phosphorene grown on Au(111) by molecular-beam epitaxy," *Phys. Rev. Mater.*, vol. 1, no. 6, pp. 1–5, 2017.

[33] W.Ma *et al.*, "Piezoelectricity in Multilayer Black Phosphorus for Piezotronics and Nanogenerators," *Adv. Mater.*, vol. 32, no. 7, pp. 1–9, 2020.

[34] Z.Zhang *et al.*, "Strain-Modulated Bandgap and Piezo-Resistive Effect in Black Phosphorus Field-Effect Transistors," *Nano Lett.*, vol. 17, no. 10, pp. 6097–6103, 2017.

[35] F.Xia, H.Wang, and Y.Jia, "Rediscovering black phosphorus as an anisotropic layered material for optoelectronics and electronics," *Nat. Commun.*, vol. 5, pp. 1–6, 2014.

[36] Y.Li, Z.Hu, S.Lin, S. K.Lai, W.Ji, and S. P.Lau, "Giant Anisotropic Raman Response of Encapsulated Ultrathin Black Phosphorus by Uniaxial Strain," *Adv.*

Funct. Mater., vol. 27, no. 19, 2017.

[37] R.Fei and L.Yang, "Strain-engineering the anisotropic electrical conductance of few-layer black phosphorus," *Nano Lett.*, vol. 14, no. 5, pp. 2884–2889, 2014.

[38] S.Lin, Y.Chui, Y.Li, and S. P.Lau, "Liquid-phase exfoliation of black phosphorus and its applications," *FlatChem*, vol. 2, pp. 15–37, 2017.

[39] X.Ling, H.Wang, S.Huang, F.Xia, and M. S.Dresselhaus, "The renaissance of black phosphorus," *Proc. Natl. Acad. Sci.*, vol. 112, no. 15, pp. 4523–4530, 2015.

[40] A.Castellanos-Gomez, "Black Phosphorus: Narrow Gap, Wide Applications," *J. Phys. Chem. Lett.*, vol. 6, no. 21, pp. 4280–4291, 2015.

[41] K.T.Lam, Z.Dong, and J.Guo, "Performance Limits Projection of Black Phosphorous Field-Effect Transistors," *IEEE Electron Device Lett.*, vol. 35, no. 9, pp. 963–965, 2014.

[42] A.Castellanos-Gomez *et al.*, "Isolation and characterization of few-layer black phosphorus," *2D Mater.*, vol. 1, no. 2, 2014.

[43] A. Morita, "Semiconducting black phosphorus," *Appl. Phys. A*, vol. 39, pp. 227–242, 1986.

[44] J. K.Burdett and S.Lee, "The pressure-induced black phosphorus to A7 (arsenic) phase transformation: An analysis using the concept of orbital symmetry

conservation," *J. Solid State Chem.*, vol. 44, no. 3, pp. 415–424, 1982.

[45] S. M.Clark and J. M.Zaug, "Compressibility of cubic white, orthorhombic black, rhombohedral black, and simple cubic black phosphorus," *Phys. Rev. B - Condens. Matter Mater. Phys.*, vol. 82, no. 13, pp. 1–6, 2010.

[46] Y.Cai, G.Zhang, and Y. W.Zhang, "Layer-dependent band alignment and work function of few-layer phosphorene," *Sci. Rep.*, vol. 4, pp. 1–6, 2014.

[47] A. N.Rudenko and M. I.Katsnelson, "Quasiparticle band structure and tight-binding model for single- and bilayer black phosphorus," *Phys. Rev. B - Condens. Matter Mater. Phys.*, vol. 89, no. 20, pp. 1–5, 2014.

[48] J.Qiao, X.Kong, Z. X.Hu, F.Yang, and W.Ji, "High-mobility transport anisotropy and linear dichroism in few-layer black phosphorus," *Nat. Commun.*, vol. 5, pp. 1–7, 2014.

[49] H.Jang, J. D.Wood, C. R.Ryder, M. C.Hersam, and D. G.Cahill, "Anisotropic Thermal Conductivity of Exfoliated Black Phosphorus," *Adv. Mater.*, vol. 27, no. 48, pp. 8017–8022, 2015.

[50] A. L.Phaneuf-L'Heureux *et al.*, "Polarization-Resolved Raman Study of Bulk-like and Davydov-Induced Vibrational Modes of Exfoliated Black Phosphorus," *Nano Lett.*, vol. 16, no. 12, pp. 7761–7767, 2016.

[51] J.Kim *et al.*, "Anomalous polarization dependence of Raman scattering and crystallographic orientation of black phosphorus," *Nanoscale*, vol. 7, no. 44, pp. 18708–18715, 2015.

[52] R. B.Jacobs, "Phosphorus at High Temperatures and Pressures," *J. Chem. Phys.*, vol. 5, no. 12, pp. 945–953, 1937.

[53] L.Li *et al.*, "Black phosphorus field-effect transistors," *Nat. Nanotechnol.*, vol. 9, no. 5, pp. 372–377, 2014.

[54] M.Nagao, A.Hayashi, and M.Tatsumisago, "All-solid-state lithium secondary batteries with high capacity using black phosphorus negative electrode," *J. Power Sources*, vol. 196, no. 16, pp. 6902–6905, 2011.

[55] M.Köpf *et al.*, "Access and in situ growth of phosphorene-precursor black phosphorus," *J. Cryst. Growth*, vol. 405, pp. 6–10, 2014.

[56] T.Nilges, M.Kersting, and T.Pfeifer, "A fast low-pressure transport route to large black phosphorus single crystals," *J. Solid State Chem.*, vol. 181, no. 8, pp. 1707–1711, 2008.

[57] K. Seibert *et al.*, "Femtosecond carrier dynamics in graphite," *Phys. Rev. B*, vol. 42, no.5, pp. 2842-2851. 1990.

[58] Q. H.Wang, K.Kalantar-Zadeh, A.Kis, J. N.Coleman, andM. S.Strano,

"Electronics and optoelectronics of two-dimensional transition metal dichalcogenides," *Nat. Nanotechnol.*, vol. 7, no. 11, pp. 699–712, 2012.

[59] G.Sansone, L.Maschio, D.Usvyat, M.Schütz, and A.Karttunen, "Toward an Accurate Estimate of the Exfoliation Energy of Black Phosphorus: A Periodic Quantum Chemical Approach," *J. Phys. Chem. Lett.*, vol. 7, no. 1, pp. 131–136, 2016.

[60] S.Wu, K. S.Hui, and K. N.Hui, "2D Black Phosphorus: from Preparation to Applications for Electrochemical Energy Storage," *Adv. Sci.*, vol. 5, no. 5, 2018.

[61] J. R.Brent, N.Savjani, E. A.Lewis, S. J.Haigh, D. J.Lewis, and P.O'Brien, "Production of few-layer phosphorene by liquid exfoliation of black phosphorus," *Chem. Commun.*, vol. 50, no. 87, pp. 13338–13341, 2014.

[62] J. O.Island, G. A.Steele, H. S. J.Van DerZant, and A.Castellanos-Gomez, "Environmental instability of few-layer black phosphorus," *2D Mater.*, vol. 2, no. 1, 2015.

[63] S.Sriram *et al.*, "Defining the role of humidity in the ambient degradation of few-layer black phosphorus," *2D Mater.*, vol. 4, no. 1, p. 015025, 2016.

[64] Z.Zhu and D.Tománek, "Semiconducting layered blue phosphorus: A computational study," *Phys. Rev. Lett.*, vol. 112, no. 17, pp. 1–5, 2014.

[65] A.Ubaldini and E.Giannini, “Improved chemical vapor transport growth of transition metal dichalcogenides,” *J. Cryst. Growth*, vol. 401, pp. 878–882, 2014.

[66] A.Ubaldini, J.Jacimovic, N.Ubrig, and E.Giannini, “Chloride-driven chemical vapor transport method for crystal growth of transition metal dichalcogenides,” *Cryst. Growth Des.*, vol. 13, no. 10, pp. 4453–4459, 2013.

[67] “Chemical vapor transport | Max Planck Institute for Chemical Physics of Solids.” [Online]. Available: https://www.cpfs.mpg.de/2651362/chemical-vapor-transport. [Accessed: 06-Jun-2019].

[68] W.Wang, H.McGregor, M.Short, and H.Zeng, “Clinical utility of Raman spectroscopy: current applications and ongoing developments,” *Adv. Heal. Care Technol.*, p. 13, 2016.

[69] J. Thomas and T. Gemming, *Analytical Transmission Electron Microscopy*, 2014th ed. Dordrecht: Springer Netherlands, 2014.

[70] S. Tardif, "Nanocolonnes de GeMn : propriétés magnétiques et structurales à la lumière du synchrotron,” Ph.D dissertation, Université de Grenoble, Français, 2011. Accessed on: Aug. 18, 2021. [Online]. Available: https://tel.archives-ouvertes.fr/tel-00585130/file/21482_TARDIF_2011_archivage_1_.pdf.

[71] M. Lee, *X-ray diffraction for materials research : from fundamentals to applications*. Oakville, ON : Boca Raton, FL: Apple Academic Press ; CRC Press, 2016.

[72] B. Voigtländer, "Atomic Force Microscopy Designs," in *Atomic Force Microscopy*, Cham: Springer International Publishing, 2019, pp. 69–86.

[73] P.Xu *et al.*, "Study of ICP-RIE etching on CdZnTe substrate," *Int. Symp. Optoelectron. Technol. Appl. 2014 Infrared Technol. Appl.*, vol. 9300, p. 93000T, 2014.

[74] C. M.Chang *et al.*, "A parametric study of ICP-RIE etching on a lithium niobate substrate," *2015 IEEE 10th Int. Conf. Nano/Micro Eng. Mol. Syst. NEMS 2015*, pp. 485–486, 2015.

[75] Z.Zhang, D. H.Xing, J.Li, and Q.Yan, "Hittorf's phosphorus: the missing link during transformation of red phosphorus to black phosphorus," *CrystEngComm*, vol. 19, no. 6, pp. 905–909, 2017.

[76] M.Wen *et al.*, "Synthesis of high-quality black phosphorus sponges for all-solid-state supercapacitors," *Mater. Horizons*, vol. 6, no. 1, pp. 176–181, 2019.

[77] M.Wen *et al.*, "Synthesis of high-quality black phosphorus sponges for all-solid-state supercapacitors," *Mater. Horizons*, vol. 6, no. 1, pp. 176–181, 2019.

[78] A. J.Watson, W.Lu, M. H. D.Guimaraes, and M.Stöhr, “Transfer of large-scale two-dimensional semiconductors: Challenges and developments,” *2D Mater.*, vol. 8, no. 3, 2021.

[79] R. J.Wu *et al.*, “Atomic and electronic structure of exfoliated black phosphorus,” *J. Vac. Sci. Technol. A Vacuum, Surfaces, Film.*, vol. 33, no. 6, p. 060604, 2015.

[80] D. D.Koleske, A. E.Wickenden, R. L.Henry, J. C.Culbertson, and M. E.Twigg, “GaN decomposition in H_2 and N_2 at MOVPE temperatures and pressures,” *J. Cryst. Growth*, vol. 223, no. 4, pp. 466–483, 2001.

[81] T. E.Haynes, W. K.Chu, T. L.Aselage, and S. T.Picraux, “Initial decomposition of GaAs during rapid thermal annealing,” *Appl. Phys. Lett.*, vol. 49, no. 11, pp. 666–668, 1986.

[82] H. K.Christenson and N. H.Thomson, “The nature of the air-cleaved mica surface,” *Surf. Sci. Rep.*, vol. 71, no. 2, pp. 367–390, 2016.

[83] W. C.Tan *et al.*, “Recent Advances in Black Phosphorus-Based Electronic Devices,” *Adv. Electron. Mater.*, vol. 5, no. 2, pp. 1–17, 2019.